A photogrammetry-based approach for soil bulk density measurements with an emphasis on applications to cosmogenic nuclide analysis

Joel Mohren*[1], Steven A. Binnie[1], Gregor M. Rink[1,†], Katharina Knödgen[1], Carlos Miranda[3], Nora Tilly[2],
5 Tibor J. Dunai[1]

[1]Institute of Geology and Mineralogy, University of Cologne, Zülpicher Str. 49b, 50674 Cologne, Germany
[2]Institute of Geography, University of Cologne, Otto-Fischer-Str. 4, 50674 Cologne, Germany
[3]Departemento de Ciencias Geólogicas, Universidad Católica del Norte, Avenida Angamos 0610, Antofagasta, Chile
10 [†]Present address: Department of Geosciences, University of Tübingen, Hölderlinstr. 12, 72074 Tübingen, Germany

Correspondence to: Joel Mohren (joel.mohren@uni-koeln.de)

Abstract. The quantification of soil bulk density (ρ_B) is a cumbersome and time-consuming task when traditional soil density sampling techniques are applied. However, it can be important for terrestrial cosmogenic nuclide (TCN) production rate scaling when deriving ages or surface process rates from buried samples, in particular when short-lived TCN such as *in situ* [14]C are

15 applied. Here, we show that soil density determinations can be made using structure-from-motion multi-view stereo (SfM-MVS) photogrammetry-based volume reconstructions of sampling pits. Accuracy and precision tests as found in the literature and as conducted in this study clearly indicate that photographs taken from both a consumer-grade digital single lens mirrorless (DSLM) and a smartphone camera are of sufficient quality to produce accurate and precise modelling results, i.e. to regularly reproduce the "true" volume and/or density by > 95%. This finding holds also if a freeware-based computing workflow is

20 applied. The technique has been used to measure ρ_B along three small-scale (< 1 km) N-S transects located in the semi-arid to arid Altos de Talinay, northern central Chile (~30.5°S, ~71.7°W), during a TCN sampling campaign. Here, long-term differences in microclimatic conditions between south-facing (SFS) and north-facing (NFS) slopes explain a sharp contrast in vegetation cover, slope gradient and general soil condition patterns. These contrasts are also reflected by the soil density data, generally coinciding with lower densities on SFS. The largest differences between NFS and SFS are evident in the lower

25 portion of the respective slopes, close to the thalwegs. In general, field-state soil bulk densities were found to vary by about 0.6 g cm^{-3} over a few tens of metres along the same slope. As such, the dataset that was mainly generated to derive more accurate TCN-based process rates and ages can be used to characterise the present-day condition of soils in the study area, which in turn can give insight into the long-term soil formation and prevailing environmental conditions. This implies that the method tested in this study may also being applied in other fields of research and work, such as soil science, agriculture, or in

30 the construction sector.

1 Introduction

Soil density determination is a time-consuming task when sampling for a terrestrial cosmogenic nuclide (TCN)-based analysis, but it is an important parameter if process rates and/or ages are inferred from the final nuclide concentration (e.g. Rodés and Evans, 2020; Rodés et al., 2011). This is because the spallogenic production rates of TCNs are typically assumed to decrease

35 exponentially with increasing depth z below the surface at a rate which is partially dependent on the sub-surface density (e.g. Dunai, 2010; Lal, 1991; Lal and Arnold, 1985; Nishiizumi et al., 1986):

$$P(z) = P_0 e^{-\rho z/\Lambda} , \tag{1}$$

where P_0 is the production at the Earth's surface and Λ denotes the attenuation length (eqn. 1 valid for non-eroding surfaces). The density ρ denotes the density of the material through which the cosmic rays traverse below the surface, i.e. the density of

40   soil, saprolite and/or rock (e.g. Heimsath and Jungers, 2013; Lal, 1991). The field-state bulk density ($\rho_{B,f}$) of a given excavated soil material is defined as

$$\rho_{B,f} = m_{e,f} V^{-1} \, , \tag{2}$$

with $m_{e,f}$ being the (field-state) mass of the excavated material and V the volume of the pit. Field-state and the corresponding dry bulk densities of soils ($\rho_{B,d}$) may vary over the larger-scale (e.g. basin-wide) erosion analysis and thus the presumption of

45   an averaged value for soil densities might be required in these cases. However, accurate knowledge about the value of $\rho_{B,f}$ and/or $\rho_{B,d}$ is more important for localised surface process rates or age inferences. The present-day soil (a term considered equivalent to regolith in this work; e.g. Heimsath et al., 1997) conditions represent only a glimpse of soil formation history, as environmental conditions, and thus the physical conditions of the subsurface, might have changed over the timescales that the cosmogenic nuclide-derived process rates integrate over (e.g. Rodés et al., 2011). Nevertheless, they represent reasonable

50   approximations, especially in scenarios of long-term steady-state erosion, i.e. where bedrock erosion equals soil production rates (e.g. Heimsath and Jungers, 2013; Heimsath et al., 1997). The imperative to obtain accurate knowledge of present-day soil densities increases if short-lived TCN, such as *in situ* [14]C, are analysed. In such a case, soil conditions are more likely to have prevailed over the timespan during which the nuclide concentration has built up. Average densities of ordinary soils range between >1.0 g cm^{-3} and 1.8 g cm^{-3} (Hartel, 2005; Manrique and Jones, 1991; Schaetzl and Thompson, 2015) but can be greater

55   or lower than this range, e.g. depending on their organic content, water content and/or degree of compaction (Schaetzl and Thompson, 2015). With respect to [10]Be production in a soil column, nuclide production (including spallogenic and muogenic production) increases by about 49% at a depth of 100 cm below the surface in a soil with $\rho = 1.1$ g cm^{-3}, when compared to a soil with $\rho = 1.8$ g cm^{-3} (*in situ* [14]C: ~32%; Fig. 1). Comparing the low density soil to a highly compacted soil, e.g. with $\rho = 2.3$ g cm^{-3} (Schaetzl and Thompson, 2015), would yield a doubling (97% increase) of the [10]Be production at 100 cm depth

60   (*in situ* [14]C: ~58%). These numbers exceed the analytical uncertainties, which are < 10% in most cases for measurements of medium to high [10]Be and *in situ* [14]C concentrations (e.g. Balco, 2017; Hippe, 2017). Thus, an accurate knowledge of local regolith densities is important for *in situ* TCN-based process rate determinations, underlining the need for a reliable, adaptable and easy-to-apply method to determine excavation densities.

    The application of photogrammetric methods to infer soil bulk densities is a relatively recent field of research and has been

65   successfully tested by Bauer et al. (2014) and Berney IV et al. (2018). Both studies found good agreements between soil densities/excavation volumes derived from traditional methods and those obtained using photogrammetry (basic concepts of photogrammetry, structure-from-motion multi-view stereo (SfM-MVS) photogrammetry, and their general application in combination with non-invasive methods in geosciences are explained e.g. in Eltner et al., 2016; James and Robson, 2012; Westoby et al., 2012). Other commonly used techniques include: the core method; the clod method; the nuclear radiation

70   method; the automated three-dimensional laser scanning method; X-ray-based methods; the thermo-time domain reflectometry (TDR) method; and non-photogrammetry excavation methods or pedotransfer functions (PTFs; for comprehensive overviews and detailed descriptions see e.g. Al-Shammary et al., 2018; Blake and Hartge, 1986; Grossman and Reinsch, 2002; Hao et al., 2008; Page-Dumroese et al., 1999; Soil Survey Staff, 2014). These approaches usually have one or more of the following disadvantages: (1) the application is time-consuming; (2) expert knowledge on the tools or programming is required; (3) large

75   amounts of sampling tools or samples are needed to be carried in the field; (4) the samples and/or the tools require a significant amount of carrying space; (5) the techniques are cost-intensive; (6) the techniques are hazardous to the applicant and/or the environment; (7) the results strongly depend on soil textures and porosity; (8) the precision of the measurements is low; (9) a prior calibration is needed.

    By contrast, the photogrammetry-based excavation method mostly seems to overcome the above-mentioned disadvantages

80   (Bauer et al., 2014; Berney IV et al., 2018). This approach can be applied to any kind of regolith whose cohesion allows the excavation of soil pits that maintain their sidewalls without collapsing (e.g. Brye et al., 2004; Maynard and Curran, 2008; Muller and Hamilton, 1992). Furthermore, it can be used in remote locations and rough terrain and does not require a significant

additional amount of material to be taken into the field. These characteristics make this technique well suited for researchers working in remote areas (in terms of distance to a storage place for samples and equipment) and whose capability for carrying sampling material is mainly based on manpower and backpack space. Such a scenario regularly applies to our TCN sampling teams of the University of Cologne, Germany, which was the reason why we tested a photogrammetric method comprehensively.

We focused on SfM-MVS photogrammetry because it is simple for non-experts to use, as most reconstruction steps are fully automated (Eltner et al., 2016). A further testing of photogrammetric methods to derive soil bulk densities from imagery acquired during fieldwork was also required, as Berney IV et al. (2018) only excavated very small volumes (~1.1 L) from flat surfaces and Bauer et al. (2014) only simulated ideal laboratory and field sampling conditions (no direct sunlight). Lighting conditions, however, have been shown to significantly affect the quality and accuracy of SfM-MVS photogrammetry-derived models (Mosbrucker et al., 2017 and ref. therein). Thus, in order to assess if the technique is applicable under fieldwork conditions during a TCN sampling campaign, we tested its accuracy and precision by simulating different lighting scenarios, parent materials, and pit orientations (i.e. dipping surfaces and vertical faces). As our intention is to contribute a method that can be adopted by the TCN community, our workflow either included the combined use of commercial and non-commercial software, or was solely based on non-commercial software (under the premise that Microsoft's Windows 10 is used as operating system). We further assumed end-users of this approach would not be experts in photography, the SfM-MVS photogrammetry technique or programming. Previous studies (e.g. Micheletti et al., 2015; Thoeni et al., 2014) have shown that the image quality of smartphone cameras can be sufficient to generate high precision models of topographic features. Thus, our tests included both a consumer grade digital, single lens, mirrorless (DSLM) camera and a smartphone camera, to assess the robustness of the method, and whether smartphone cameras can be used as substitutes for higher-grade models with regards to the accuracy and precision of $\rho_{B,f}$ determinations. Finally, we applied the method during a TCN sampling campaign in the Coastal Cordillera of northern central Chile, where we investigate the impact of aspect-related differences in microclimate and vegetation on Earth-shaping processes and the formation of topography along narrow transects (cf. Bernhard et al., 2018; Gutiérrez-Jurado and Vivoni, 2013a, b; Oeser et al., 2018). Therefore, soil densities were derived, initially to scale soil production rates inferred from saprolite TCN concentrations (e.g. Heimsath and Burke, 2013) across contrasting slope aspects. However, due to the simple and time-efficient application of the method, we extended our dataset of regolith densities along the respective slopes in order to study aspect-related differences in this particular soil property.

2 Methods

2.1 Imaging testing scenarios, part 1: simulating a soil pit

To evaluate the accuracy and precision of the SfM-MVS photogrammetry-based excavation method and to test convenient workflows to obtain values for $\rho_{B,f}$ and $\rho_{B,d}$, we adopted a two-phased testing procedure (Fig. 2). The first phase consisted of the simulation of a soil pit. For this we used the interior of a square flowerpot, on top of which a board was attached, imitating a soil surface. Into the board we cut a square hole that would fit the opening of the flowerpot (Fig. 3 and supplement). The hole could be covered by a thin fabric cover to simulate the pre-dug surface; removing the fabric cover would simulate the pit after digging, measuring 22 x 22 x 23 cm (width x length x depth; Table 1). The cubic shape of the flowerpot differs from that of a semi-circular pit, which has been found to be the optimal shape to reconstruct the surface of the pit using SfM photogrammetry (Berney IV et al., 2018).

However, the testing setup was designed in a way that it would contain features that might play a role during a field campaign and could potentially impede a proper SfM-MSV photogrammetric reconstruction. Examples are steep pit sidewalls, which can also cause strong shading inside the pit and a lack of image texture, e.g. caused by featureless areas (Gruen, 2012; James and Robson, 2012). For our tests, the latter needed to be improved by painting black/dark brown and white patterns on the flat

and initially dark grey sidewalls of the artificial pit and on the pre-dug surface. We further sealed the contact surface between flowerpot and board using white silicone glue. This was necessary in order to be able to determine the reference volume of the test pit by filling it with water, which we repeated ten times (assuming $\rho_{H2O} = 1$ g cm^{-3} for demineralised water at ~20°C; assumption holds for all water-based reference volume determinations conducted in this study). An advantage of this type of testing scenario over those used by Bauer et al. (2014) and Berney IV et al. (2018) is that the test pit could be transported to various locations, simulating different lighting conditions and orientation scenarios. Inside the facilities of the Institute of Geology and Mineralogy at the University of Cologne, images were acquired with artificial lights (ceiling lighting) and/or windows being the main illumination sources. Outside of the facilities, further set ups included cloudy and sunny conditions, where the pit was either exposed to direct sunlight or being shadowed. The pit was also tilted to up to 90°, to simulate the sampling of sediment wall faces, i.e. cavities.

In scenarios representing regular pit-sampling, i.e. on even or slightly tilted surfaces, typically 24 pictures were taken horizontally in ~45° steps and vertically at angles of ~25° (at a height of about 80 cm), ~50° and ~90° (both at heights of about 150 cm) to cover all surfaces within the pit; an equal procedure was applied to photograph the pre-dug surface. The distance between the camera lens and the pit was kept constant to make the imagery data as comparable as possible between the sites. For vertical pit volume determinations, imagery was acquired parallel to the surface in an upward/downward and lateral move (about 30 to 40 pictures in total per setting). Additionally, non-surface parallel pictures were taken to image the sidewalls. In general, we aimed for taking at minimum three pictures per surface to allow good image matching results (James and Robson, 2012).

In all testing scenarios (including field tests; Section 2.2), we used 3-4 dice on which the dots served as markers and placed 3 photographic 10 cm long reference scales into the scene. If no ground control points (GCP) with known reference coordinates are available, the most accurate scaling is achieved by placing a scale that spans over the length of the object of interest (e.g. James and Robson, 2012), as was done by Bauer et al. (2014) and Berney IV et al. (2018), who placed a frame around the soil pits. In the field, however, when the decision about the extent of a pit may needs to be adopted to local constrains (e.g. regolith depth, vegetation cover), such a construction may not be applicable. A further advantage of the photographic reference scales is that they can be used in different (or changing) lighting conditions due to their strong contrasts and that they can be placed at the outer rims and the centre of the respective scene. Pictures were taken initially from the pre-dug surface and afterwards from the pit/cavity to reconstruct a closed and watertight model of the excavation.

Besides using a consumer-grade DSLM camera [Olympus OM-D E-M10, 16 megapixel (MP); Lumix G 50 mm in 35 mm film equivalent f1.7 aspherical fixed focal length lens] we also took pictures using the main camera of a Sony Xperia Z5 Compact (23 MP, 24 mm in 35 mm film equivalent f2.0 fixed focal length lens). Lens type, dynamic range and image resolution of the DSLM camera used here can be considered to be sufficient for accurate close range SfM-MVS photogrammetry-based modelling (for an overview on camera hardware requirements see Berney IV et al., 2018; Eltner et al., 2016; Mosbrucker et al., 2017; Smith et al., 2016). Intentionally, this camera was bought to document geomorphological fieldwork campaigns and not for the purpose of any photogrammetric application. We presume that comparable camera models are currently taken to the field by geoscientists during their TCN sampling campaigns, where impromptu volume determinations of sampling pits may be required. Using the DSLM camera, the pictures were taken in P-Mode and saved in RAW file format, which preserves a higher information capacity than does the JPEG image format (Mosbrucker et al., 2015). Photographs from the smartphone were taken in manual mode (leaving all settings in automatic mode; Android ver. 7.1.1) and could only be saved in JPEG file format (highest resolution).

2.2 Imaging testing scenarios, part 2: field tests

During a second testing phase, a similar imaging using the same cameras was applied for field tests on four soil pits and one loess wall cavity. The field tests were conducted in July 2017 in a gravel pit located approximately 35 km to the west of

Cologne, Germany (51.0°N, 6.4°E). Here, gravels belonging to the body of a mid-Pleistocene main terrace of the Rhine river are overlain by a ~11 m thick sequence of Middle to Late Pleistocene loess deposits and intercalated soils, capped by Holocene soil (Kels, 2007). The gravels are exploited under dry mining conditions. At the outer fringes of the gravel pit, the overburden loess has mostly been removed, leaving the undisturbed uppermost layers of the Pleistocene gravels overlain by a cap of 0 cm
170   to ~10 cm of loess. At the outermost rims of the gravel pit, the uppermost ~4 m of the loess overburden are accessible. As such, the area provides excellent conditions to test the SfM-MVS photogrammetry-based soil bulk density approach on (1) the homogeneous loess and (2) gravels situated in a sandy/silty matrix. Similar to the tests on the artificial pit, this testing environment also provided difficult conditions for the application of the SfM-MVS photogrammetric method, such as potentially disturbing vegetation, heavy shadowing and – in the case of excavations conducted into the loess – partially low
175   image texture (Gruen, 2012; James and Robson, 2012). Due to the rough surfaces of the sidewalls of the pits dug into the gravels, areas could be shielded from view by protruding clasts and thus not be captured by the photography (Berney IV et al., 2018). During photographing, weather conditions were mostly sunny, occasionally interrupted by more cloudy episodes (Table 4).

Three pits (BD17-P01, -P06, -P11) were dug into the gravel (Fig. 4), while BD17-P12 was dug into a ~12° southward dipping
180   mine access ramp consisting of compacted loess. All four pits were dug within a radius of ~20 m. BD17-P13 was dug about 60 m to the north into the foot of a ~4 m high loess wall. BD17-P01 and -P06 were small pits with a surface area of approximately 20 x 20 cm (depth: ~25 cm), while BD17-P11 and -P12 were about 60 x 60 cm in size (depth: ~50 cm). BD17-P06 was located on a ~13° eastward dipping surface. The cavity dug into the loess wall (BD17-P13) measured approximately 40 x 15 x 15 cm (width x length x depth). All excavations were conducted using a spade and a pickaxe. The excavated material
185   was placed on a tarp and the mass of both was determined using an ordinary luggage scale (E-PRANCE, max. 50 kg, d = 0.01 kg). The excavated material of BD17-P01, -P06 and -P13 were also weighted in the laboratory.

From BD17-P11 and -P12 we took pictures during the morning/noon and the afternoon hours to compare the results under different lighting conditions and to assess the reproducibility of the calculated volumes and densities (BD17-P11m, -P11a, -P12m, -P12a). The sampling locations of BD17-P11 and -P12 were chosen in a way that the surrounding vegetation would
190   cause shading of the excavated pit during the afternoon hours. Furthermore, we placed a boulder into these pits to investigate the possibility of detecting the volume change in the respective models (BD17-P11.1m, -P11.1a, -P12.1m and -P12.1a; see supplement). The reference volume of the boulder ($V_{b,ref}$) was determined by submerging it into water, applying Archimedes' principle (6 repetitions). To obtain an independent measure of the volume of the excavated pits (the reference volume, V_{PU}) we filled them using polyurethane foam (PU foam) as described by Brye et al. (2004) and Muller and Hamilton (1992). In
195   addition, polystyrene was used to reduce consumption of the PU foam in the large pits BD17-P11 and –P12. In the facilities of the UoC, the negative casts were put into watertight bags and submerged under water to determine the respective values for V_{PU}, applying Archimedes' principle. The cast of BD17-P01 was submerged 11 times, that of BD17-P06 five times and that of BD17-P13 six times to measure the reference volume precision. In addition, we applied the core method by taking volumetric samples (100.0 ± 0.5 cm^3) from the larger pits (BD17-P11, $n = 8$ incl. duplicates; and -P12, $n = 6$ incl. duplicates)
200   and the loess wall (BD17-P13, $n = 3$), using soil sample rings to derive bulk densities independently from the PU foam/polystyrene-based volume of the excavations (Fig. 2). These samples were oven-dried at 105°C overnight to constant weights to calculate the dry bulk density $\rho_{B,d}$. The excavated material of BD17-P01, -P06 and -P13 was air-dried for several weeks and afterwards treated in a similar fashion as the sample ring samples to derive the dry masses ($m_{e,d}$).

2.3 Computer-based workflow

205   We tested different approaches to derive the SfM-MVS photogrammetry-based pit volumes on the computer. For such computer-based work, three main factors are important to make the method and workflow we test here feasible for a broad range of applications: (1) duration of processing, (2) costs and (3) expertise of the user. As such, we aimed at deriving a

workflow that relies entirely (except for the operating system) on freeware computer programs ("freeware workflow"; a detailed protocol on the computing steps is provided in the supplement) as well as one that might be a more convenient to apply, but which involves commercial software ("performance workflow"; Fig. 5). Both workflows are based on Windows-compatible computer programs that do not require special knowledge neither in programming nor in photography and photogrammetry (for a detailed description on the individual computing steps see Smith et al., 2016). The computer we used for testing purposes was a Dell Precision Tower 3620 (3.60 GHz processor, 64 Gb RAM, Intel HD Graphics 630 on-board and NVIDIA Quadro M4000). Although this machine can be considered to be above average in terms of computing and graphics (year 2020), we note that most processing steps were carried out in the background while working with other, memory- and/or graphics-demanding software, such as ArcMap (ver. 10.6), Google Earth Pro (ver. 7.3.3), Microsoft Office 2016 and others.

In general, we modelled the pre-dug surface and the pit separately and aligned and merged them afterwards. Water tightness, a prerequisite to derive the volume of the final model, was achieved by automatically bridging the gaps of the merged mesh. Other approaches, such as deriving a single model from the pre-dug surface and the pit point clouds using the poisson surface reconstruction (Kazhdan et al., 2006; Kazhdan and Hoppe, 2013) led to the appearance of large bumps in the model if the surface roughness of the pit was too high. For example, poisson surface reconstruction did not create an accurate but bumpy surface of the boulder placed into the pits of scenarios BD17-P11.1 and -P12.1, most likely due to bad orientation of the face normals. In addition, various manual adjustments were required, such as a re-orientation of face normals, to get appropriate results even for more easy-to-model settings. Thus, we chose to reconstruct the pre-dug and the pit surfaces parallel and merged the final meshes afterwards. The model outcomes were visually checked for irregularities such as uneven surfaces, holes and bumps. As long as these features did not reflect large deviations from the reference shape, we accepted the respective model for further data analysis.

For the freeware workflow, we used the programs Regard3D (ver. 1.0.0) to build point clouds and meshes and CloudCompare (ver. 2.11) to scale the pit model and to align and merge it with the pre-dug surface (for an overview on other photogrammetry software available see Eltner et al., 2016; Smith et al., 2016). We chose these programs because we find them straightforward to use and both come with a comprehensive documentation. All the steps listed above can be carried out in Agisoft Metashape Pro (ver. 1.6.1), which is the main (commercial) program used in the performance workflow and which has been widely used for applications in geoscience (Eltner et al., 2016). The software also allows for batch processing and supports graphics processing unit (GPU) acceleration. For all modelling performed in this study using Agisoft Metashape Pro, we used either the integrated (testing scenarios) or the additionally installed (AT17/18 sampling campaign, Section 2.4) graphics card for GPU acceleration.

In both the performance and freeware workflows, the final step was to bridge the edges of the reconstructed pre-dug surface and the pit to water tighten the models, which was achieved using Microsoft 3D Builder (ver. 18.0.1931.0). Regard3D requires pictures in the JPEG file format as input, while Agisoft Metashape can process TIF files, which contain a higher information capacity than do JPEG files (Mosbrucker et al., 2015). The images taken using the DSLM camera in the RAW file format were converted accordingly. While running both workflows, we recorded the time that was required to finally determine the volume (using e.g. CloudCompare or Meshlab, ver. 2016.12). Photographs were not post-processed (an overview on some possibilities for post-processing are summarised in Mosbrucker et al., 2017) before using them for the SfM-MVS photogrammetric reconstruction to keep the workflow as simple as possible.

We always aimed at leaving the default parameters for the respective processing steps, which worked fine in the majority of the cases, especially for the field tests. This included poisson surface reconstruction octree depth (Kazhdan et al., 2006; Kazhdan and Hoppe, 2013) in Regard3D (default: 9) and the cloud densification/meshing accuracy (default: medium) in Agisoft Metashape, mainly because meshes generated from both the freeware and the performance workflow would be comparable in detail and file sizes (in general < 10 Mb). Agisoft Metashape is able to automatically detect markers placed within a given set of aligned photographs. For the tests on the artificial pit using the smartphone camera (D17 to D26), we thus

marked the photographic reference scales with pairs of black circles, located at a known distance from each other, to test if this could speed up the processing.

2.4 Soil bulk density transects from the Altos de Talinay, northern central Chile

The experience obtained during the testing phase was important in applying SfM-MVS photogrammetry for expedient soil
255 bulk density analysis along N-S oriented TCN sampling transects spanning the slopes of three E-W running valleys (C1, C2, C5; Fig. 9) in the Altos de Talinay. Geographically, the study area is part of the Coastal Cordillera of northern central Chile (30.5°S; 71.7°W). The main aim of the TCN sampling campaign, which was conducted in March 2018, was to derive process rates (erosion and soil production; e.g. Dunai, 2010; Heimsath and Jungers, 2013) from concentrations of cosmogenic nuclides in sediments and bedrock/saprolite. In this generally arid to semi-arid study area (e.g. Gutierrez et al., 2010; López-Cortés and
260 López, 2004), north-facing slopes (NFS) tend to be flatter and less densely vegetated then their south-facing counterparts (SFS), which show greater regolith depths and are generally subject to intense bioturbation (cf. Gutiérrez-Jurado and Vivoni, 2013a, b). The type of vegetation differs between xeric shrubland on the NFS and evergreen sclerophyll shrubs on the SFS (Armesto and Martínez, 1978; and own observations). The major soil types found in the study area are Entisols and Aridisols (Casanova et al., 2013). The soils are situated on intrusive rocks (melanocratic facies containing dioritic protolith rocks,
265 intruded by leucocratic granitoid dykes; Emparan and Pineda, 2006; Gana, 1991; and own observations) with a mean density ρ_{BR} of 2.82 ± 0.11 g cm^{-3}, as measured by submerging bedrock and unweathered saprolite samples ($n = 28$) from catchment C5 under water.

We obtained soil density data from in total 69 soil pits dug into diffusively-eroding slope noses and ridgetops, using a spade, a hand shovel and a pickaxe. The soil pits were located within a distance of about 25-50 m from each other. As soil bulk
270 densities are strongly influenced by biotic activity and plant cover, among others (for an overview see e.g. Al-Shammary et al., 2018 and references therein), the densities as measured using the SfM-MVS photogrammetry-based technique should reflect aspect-related differences in the study area. To acquire the imagery, we used two different DSLM cameras: the Olympus E-M10 (14-42 mm f3.5-5.6 lens, pictures mostly taken at 14 mm, i.e. 28 mm in 35 mm film equivalent), which was also used in the tests described in ch. 2.1.1 and 2.1.2 with a different lens, and a Panasonic DMC-GX80 (16 MP; Lumix G 40 mm in
275 35 mm film equivalent f1.7 aspherical fixed focal length lens). Automatic mode was used for both cameras for taking the pictures, which were saved in JPEG file format (highest resolution). The imaging technique was based on the experiences made during the test phase, so we took care of covering all surfaces at least three times and included close ups (avoiding using optical zoom, e.g. Smith et al., 2016). To enhance the image texture, a brush was used to clean the bedrock/saprolite layer at the bottom of the respective pit. At most sites, 3-4 dice and 2-3 scale bars were placed for referencing and scaling purposes.
280 Weather conditions were either sunny or cloudy; photographs were taken between 10:30 am and 06:30 pm. Similar to the BD17 field tests, the excavated material was put on a tarp to measure its weight using a hand balance (KERN 50K50, d = 50 g). The weight of the tarp was later subtracted from the final mass of the excavated material ($m_{e,f}$). All computing steps were conducted using a Gigabyte Z87-D3HP-based computer (3.10 GHz processor, 16 Gb RAM, Intel HD Graphics 4600 on-board and NVIDIA GeForce GTX 760) with no other memory- and/or graphics-demanding software running simultaneously.
285 Although we tested the accuracy and precision of the SfM-MVS photogrammetry-based density estimation before this fieldwork was conducted, we decided to further test the reliability of the technique in the field by a stepwise volume determination in three pits (AT17-001, -028 and -029; all pictures used to derive soil bulk densities in this study have been taken during March 2018). In detail, we dug the pit until the saprolite or bedrock was reached and applied the usual workflow to measure the weight of the excavated material and to take the pictures needed for the photogrammetric reconstruction. In the
290 case of a stepwise volume determination, we then further dug into the saprolite, again weighing the mass of the excavated material and taking another set of pictures from the deepened pit. This method allowed for the photogrammetric reconstruction of three models: (1) the shallow pit; (2) the deepened pit and (3) the "void" between the ground surfaces of the shallow and

the deepened pits. By applying the performance workflow to all three models independently from each other, we could test if the volume determination is internally consistent, i.e. if the sum of the volumes of (1) and (3) equals the total volume of (2).

295   In addition to these tests, we dug two pits located close to each other (~1 m) but reaching different depths into the regolith layer in order to compare their values for $\rho_{B,f}$. We expected these to be similar in the weakly developed soils of the study area (AT17-032, 10 cm and -032TS, 5 cm). A similar approach was applied at sample sites AT18-102(1) and AT18-102(2), where we dug 28 cm (soil/saprolite) and 3 cm (soil only) into the ground, respectively. Here, our intention was to test if a clear and significant change in density could be measured.

300   For most sampling sites where we took our TCN samples, we also aimed for sampling a small (~330 g on average) but representative column of regolith covering the entire profile of the respective pits. This material was used to assess the gravimetric water content and the mass of the fraction > 2 mm of the soils. Soil densities are affected by the water content of the soil and the presence of larger clasts in the sample and are thus commonly corrected for both variables by drying the samples and removing the > 2 mm fraction in order to measure dry soil densities (ρ_d, e.g. Blake and Hartge, 1986; Soil Survey

305   Staff, 2014). Although the determination of $\rho_{B,f}$ is likely sufficient for a correction of TCN production rates in arid zones, in some cases it might be necessary to infer $\rho_{B,d}$, especially if the samples were taken during wet season. In addition to that, the method might also be used to infer comparable values of ρ_d in non-TCN related applications. Thus, we used the aliquot samples to calculate the conversion factors f_d [conversion to calculate the oven-dried mass of the excavation as applied by Blake and Hartge (1986) for the clod method], $f_{r,d}$ (conversion to remove the mass of the > 2 mm fraction from the oven-dried excavated

310   mass) and $f_{r,V}$ (conversion to remove the volume of the > 2 mm fraction from the excavated volume),

$$f_d = m_{a,d} m_{a,f}^{-1} , \tag{3}$$

$$f_{r,d} = 1 - \left(m_{a,r} m_{a,d}^{-1} \right) , \tag{4}$$

$$f_{r,V} = 1 - \left[V_{a,r} \left(m_{a,d} \rho_{B,d}^{-1} \right)^{-1} \right] , \tag{5}$$

with $m_{a,f}$ being the field-state mass of the aliquot sample, $m_{a,d}$ its oven-dried mass, $m_{a,r}$ the mass of the fraction > 2 mm and

315    $V_{a,r}$ the Volume of the rocks in the aliquot sample (cf. Russo, 1983; Soil Survey Staff, 2014; Vincent and Chadwick, 1994). $V_{a,r}$ could either be measured, e.g. by submerging the clasts under water, or it can be derived by using the bedrock density ρ_{BR}, which would equal the assumed density of the clasts (Brye et al., 2004; Grossman and Reinsch, 2002; Russo, 1983; Vincent and Chadwick, 1994). While eqn. (4) assumes that the > 2 mm fraction is free of moisture, eqn. (5) assumes that the clasts in the soil pits are separated by < 2 mm material or contact between the > 2 mm clasts is minimal (Grossman and Reinsch, 2002).

320   To ensure that water loss after sampling would be minimised (e.g. Blake and Hartge, 1986), the sampling material of the aliquots ($n = 37$) was sealed in plastic bags and stored at a cool and shaded place during fieldwork and in an air-conditioned room afterwards. Further processing, i.e. drying, sieving, weighing and determining $V_{a,r}$ by submerging the clasts in a water-filled volumetric flask, was performed in facilities of the Universidad Católica del Norte, Antofagasta, Chile. With the regard to the general formula for ρ, defined as mass per volume, inserting (3) in (2) yields

325    $$\rho_{B,d} = \left(m_{e,f} m_{a,d} m_{a,f}^{-1} \right) V_{SfM}^{-1} , \tag{6}$$

to approximate the dry bulk density. Accordingly, the dry soil density can be approximated by inserting (3), (4) and (5) into (2), yielding

$$\rho_d = \left[\left[(m_{a,d} - m_{a,r}) m_{a,f}^{-1} \right] m_{e,f} \right] \left[1 - \left[V_{a,r} \left(m_{a,d} \rho_{B,d}^{-1} \right)^{-1} \right] V_{SfM}^{-1} \right]^{-1} , \tag{7}$$

and thus, providing the possibility to approximate comparable soil densities using a combination of the SfM-MVS

330   photogrammetry-based method and representative regolith sampling.

3 Results

3.1 Volume inferences from the artificial pit

In total, 16 settings were pictured using the DSLM camera and 10 settings using the smartphone (Fig. 6, Table 2). For all scenarios but two (D09 and D23), the applied performance workflow yielded visually matching modelling reproductions of the inside of the flowerpot. Regarding the freeware workflow, default processing settings had to be adjusted in the majority of cases to generate the surfaces. This predominantly applied to the point cloud densification step of the pits in Regard3D, which was mostly carried out using the multi-view environment (MVE) method (Fuhrmann et al., 2014) instead of the default patch-based and clustering multi-view stereo algorithms (CMVS/PMVS; Furukawa and Ponce, 2009). The latter often failed to densify the point cloud in shadowed and/or dark areas of the artificial pit. In 19 out of 41 successfully created models netfabb Basic (freeware; ver. 7.4.0) had to be used to bridge one edge of pre-dug surface to an edge of the pit mesh manually (< 1 min of additional processing time required). This step was necessary in those cases where the meshes of pre-dug surface and pit did not overlap at any point, i.e. were no connection was established beforehand. However, five freeware-scenarios (D05, D09, D12, D18 and D23) failed to yield acceptable watertight meshes. For those scenarios where the modelling was successful, the derived volumes differed on average about -0.7% (performance, DSLM), -0.6% (performance, smartphone), -3.4% (freeware, DSLM) and -0.3% (freeware, smartphone) from the respective reference volumes. The maximum recorded difference was -6.5%, calculated for D14 applying the freeware workflow.

In general, the volumes derived using this workflow showed a lager variability (203 cm^3 using the DSLM and 281 cm^3 using the smartphone) than the performance workflow (70 cm^3 using the DSLM and 124 cm^3 using the smartphone). Average processing durations ranged between 25 min and 30 min for all workflows and cameras applied (see Table B1). However, the effective time of non-automated, i.e. manual processing was twice as large for the performance workflow (~15 min) than for the freeware workflow (8 min). A clear advantage of the performance workflow is the ability of performing batch processing in Agisoft Metashape, while attendance of the user is required after each processing step in Regard3D.

3.2 Volumes and densities obtained from the field tests

The reference PU foam-based method (Section 2.2) yields consistent field-state bulk densities for BD17-P01 and -P06 (~2.12 g cm^{-3}). The highest value of $\rho_{B,f}$ is measured for BD17-P11 (2.34 ± 0.01 g cm^{-3}). In contrast to that, lower values are obtained for the loess pit BD17-P12 (1.90 ± 0.01 g cm^{-3}) and the loess cavity BD17-P13 (1.54 ± 0.03 g cm^{-3}). PU foam/polystyrene-derived field densities significantly differ from those derived using soil sample rings (Table B3) in two out of three sites. Only at site BD17-P12 the respective values (PU-foam 1.90 ± 0.01 g cm^{-3}; sample rings 1.82 ± 0.08 g cm^{-3}) overlap. However, close values are also obtained for site BD17-P13, especially when the oven-dried masses $m_{e,d}$ (dried excavation) are used to calculate $\rho_{B,d}$ (PU foam 1.51 ± 0.03 g cm^{-3}, sample rings 1.35 ± 0.09 g cm^{-3}). $V_{b,ref}$ was measured to be 6116 ± 63 cm^3. We subtracted this value from the PU foam cast-derived measurements of sites P11 and P12, yielding volumes of 93789 ± 326 cm^3 and 88959 ± 326 cm^3, respectively (error propagation in this study by adding uncertainties in quadrature). Concerning the SfM-MVS photogrammetry-based pit reconstructions, modelled volumes show a high correlation with the reference volumes (R² = 0.98; Fig. 7). For the pits BD17-P01, -P06, -P11, -P12, and -P13, the deviations from the reference volumes range between -8.7% and +13.8% (Table 4). 16 out of 28 modelled volumes differ less than 5% from the respective reference values. In most cases, the freeware workflow yields the largest deviation within a given setting (BD17-P01, -P06, -P11a, -P12). In all settings except for BD17-P11, the difference is below 8%. Like at most other sites, the large deviations in that particular setting show little variabilities (+8.2% to +11.1% for P11m and +10.5% to +13.8% for P11a).

As indicated by the results obtained from the tests using the artificial pit, volumes based on images taken from the DSLM and the smartphone are very consistent when the performance workflow is applied. Consequently, calculated densities are very

similar at each site (average difference is ~0.02 g cm^{-3}); DSLM/freeware and smartphone/freeware workflow-derived densities are slightly less consistent (average difference ~0.04 g cm^{-3}).

The reconstruction of the modified pits BD17-P11.1 and -P12.1 yielded more accurate and precise results for the performance workflow than for the freeware workflow (Table 5). Mean values for the boulder ($V_{b,sfm}$), calculated by subtracting the volumes of the standard pits from the corresponding modified pits, are 6262 ± 1300 g cm^{-3} (DSLM imagery) and 6264 ± 97 g cm^{-3} (smartphone photographs; here, errors represent the standard deviation of the mean without including measurement uncertainties). In contrast to that, mean freeware-based volumes are 4450 ± 2199 g cm^{-3} and 6842 ± 2012 g cm^{-3} for DSLM and smartphone images, respectively.

The large differences between the modelled volumes of BD17-P11 and the corresponding values for V_{PU} are also reflected in the final values for $\rho_{B,f}$ (Fig. 8). Deviations from the reference range between -0.18 g cm^{-3} and -0.28 g cm^{-3} with the latter being the maximum difference recorded in this test. 15 out of 28 calculated densities differ by less than 0.1 g cm^{-3} from the reference density. The average difference is lowest for the DSLM/performance workflow (0.09 g cm^{-3}) and the smartphone/performance workflow (0.11 g cm^{-3}). The DSLM/freeware and smartphone/freeware workflows yield average differences of 0.12 and 0.13 g cm^{-3}, respectively. However, these values are strongly affected by generally large deviations reported for site BD17-P11. If only the remaining sites BD17-P01, -P06, -P12 and -P13 are considered, mean differences decrease to 0.05 g cm^{-3} (DSLM/performance) and 0.06 g cm^{-3} (all others). The application of sample rings generally yielded lower densities than the SfM-MVS photogrammetry-based densities (Tables 3 and 4). However, the obtained mean values are very similar to those derived using SfM-MVS photogrammetry, and partially overlap within their error ranges at sites BD17-P12 and -P13. Using the $m_{e,d}$ to calculate $\rho_{B,d}$, densities decrease by about 0.08 g cm^{-3} (BD17-P01), 0.03 g cm^{-3} (BD17-P06) and 0.04 g cm^{-3} (BD17-P13), respectively (see Table B2).

It took on average 53 min from uploading the pictures to obtain the final pit volume when the DSLM/performance workflow was applied and 68 min for the smartphone/performance workflow (see Table B1). This was faster than the average durations recorded for freeware workflows (85 min using the DSLM pictures and 86 min using the smartphone pictures). A regularly applied deviation from the default settings of the freeware workflow was the adjustment of the matching keypoint sensitivity in Regard3D, which in most cases had to be lowered to save computing time. In the case of the modified pits BD17-P11.1 and -P12.1, 3-9 additional pictures taken from different horizontal angles (but same distance to the object) had to be added in order to reconstruct the shape of the boulder placed inside the respective pits more properly.

As already noted for the tests carried out using the artificial pit, the working steps requiring intensive manual adjustments take less time for the freeware workflows (17 min on average) than the performance workflows (26 min using the DSLM pictures and 32 min using the smartphone photographs).

3.3 Altos de Talinay sampling transects

During the fieldwork conducted in March 2018, we took on average ~50 pictures per site (n = 69; see supplement). In contrast to the image acquisition as conducted during the test phase, when an equal amount of pictures was taken from the pre-dug surface and the pit (about 50-60 pictures per site in total), we mainly focused on the pit as it has shown to be more important but also more difficult to reconstruct. However, also 30 or less pictures in total were sufficient to generate watertight models accurately reflecting the original pit.

On average, mean processing durations (57 min to obtain one density value) were close to those reported for the BD17 field tests (DSLM/performance workflow; see Table B1). Difficulties during processing mainly arose during the alignment of the pre-dug surface mesh and the pit model, if the ground had not been sufficiently cleared from vegetation before the pit was dug or if the radius of clearance work around the pit was not large enough. In these cases the (manual) scanning for matching reference points was complicated on both models; the contribution of this step to the total processing time consumption was

on average 11 min (19%), a bit higher than recorded for the BD17 field test (8 min or 15 % for the DSLM/performance workflow).

The stepwise volume quantification of the three test sites yielded deviations of +49 cm^3 (AT17-001), -545 cm^3 (AT17-028) and +280 cm^3 (AT17-029), when compared to the total volume obtained from the finally deepened pit (Table 6). The resulting differences in $\rho_{B,f}$ would be 0.01 g cm^{-3} for AT17-001, 0.05 g cm^{-3} for AT17-028 and 0.04 g cm^{-3} for AT17-029. The duplicate soil densities analysed in pits AT17-032 and -032TS are very similar (1.65 ± 0.05 cm^{-3} and 1.68 ± 0.07 g cm^{-3}, respectively), while the density of the soil/saprolite mix of AT18-102(1) is twice as large as that of the soil layer in AT18-102(2) alone (1.84 ± 0.01 g cm^{-3} vs. 0.91 ± 0.04 g cm^{-3}).

Regarding the entire AT17/18 dataset, field-state bulk densities as obtained from the performance workflow range between 0.91 ± 0.00 g cm^{-3} (AT17-026) and 2.11 ± 0.01 g cm^{-3} (AT18-154; see supplement for a detailed list). Averaged bulk field densities differ by 0.18 g cm^{-3} (C1), 0.16 g cm^{-3} (C2) and 0.04 g cm^{-3} (C5) between the north- and south-facing slope of the respective transects (Table 7). The differences are, however, not significant, considering the standard deviations of 0.12 g cm^{-3} to 0.19 g cm^{-3} (standard deviations do not incorporate measurement uncertainties of the individual measurements). A high variability in terms of excavation masses and pit volumes was mainly due to differing soil depths but also constrained by local, site-specific features, such a vegetation cover and/or slope angle.

Although mean soil depths are generally lower on north-facing slopes than on their south-facing counterparts, no correlation between soil depth and field bulk density is ascertainable. The average ridgetop value for $\rho_{B,f}$ (1.49 ± 0.29 g cm^{-3}) is close to the mean value for all densities of the dataset, which is 1.47 ± 0.19 g cm^{-3}. With respect to the location of the individual sampling sites it is striking that large contrasts along the respective sampling transects are especially evident within the lower portion of the slopes, i.e. areas located closer to the thalwegs which are steeper than the upslope areas (Fig. 9,10).

The determination of gravimetric regolith water contents from the 37 aliquot samples reveals that the soils of both north- and south-facing slopes were notably dry during the time of sampling (March 2018), as most values for f_d range between 0.98 and 0.99. Therefore, the resulting dry bulk densities differ not significantly from the field-state bulk densities (maximum difference of the means is ~0.03 g cm^{-3}; Table 8). In catchment C5, mean values for $\rho_{B,f}$ are higher on the SFS than on the NFS when only the small dataset is considered ($n = 11$ for C5). With regard to all catchments, the inferred mean values for ρ_d are up to 0.25 g cm^{-3} lower than $\rho_{B,f}$ (NFS C2). The uncertainties of the respective values for ρ_d range between 4% and 11% (see supplement). We used ρ_{BR} to calculate $V_{a,r}$, as the aliquot sample sizes were too small for some sites, causing large relative errors when $V_{a,r}$ was measured by submerging the > 2 mm fraction under water. The lowering of the mean values, however, occurs similarly on both slopes within the respective catchments.

4 Discussion

4.1 Accuracy and precision of SfM-MVS photogrammetry-based soil pit volume determination

The tests performed on the artificial pit show that accurate and precise results (regularly < 5% deviation from the reference volume) are obtained from applying both the performance and the freeware workflow. (Day-)Lighting conditions and picture file formats seem not to significantly affect the overall availability of the computer algorithms used to model the surfaces, which is further supported by the satisfying reconstruction of all BD17 and AT17/18 pits, the latter analysed under fieldwork conditions. Also the imaging strategies, cameras and workflows applied in this study are sufficient to obtain reliable results for the objects and scales being analysed. Difficult-to-reconstruct settings are more likely being properly modelled using Agisoft Metashape than using Regard3D. The failure of reconstructions, which occurred only for the tests conducted on the artificial pit, was related to a combination of low image textures and bad picture coverage of surfaces (e.g. Gruen, 2012; James and Robson, 2012).

Similar to the findings of Micheletti et al. (2015), the scatter of the testing results shown in Figure 6 is slightly larger for models created from smartphone pictures than from the DSLM camera. One reason for this finding is likely the fact that pictures were taken through a built-in wide-angle lens when the smartphone was used. As a result, perspective distortion was greater than on the pictures taken with the DSLM camera, thereby affecting the photogrammetric reconstruction (Neale et al., 2011). However, a larger difference in data scatter is found between the two workflows applied rather than in the camera type used. The faster but less accurate scaling procedure is very likely one of the main factors causing less precise results when applying the freeware workflow. In general, image characteristics have been identified as one of the most important factors affecting the accuracy of SfM-based modelling (e.g. Mosbrucker et al., 2017). In the freeware workflow, this factor is, in terms of precision, likely to be less important than the scaling procedure, as scaling is performed by measuring the distance between two points on a photographic reference scale as reconstructed in the textured mesh of the pit. Thus, the quality of the reconstructed mesh surface, i.e. its surface roughness, and the accurateness of the texture fit on the model can lead to an increase or decrease of the straight connection line between the measuring points. This provides an explanation for the scatter of the data obtained from the testing scenarios, which, however, can be considered being still tolerable for TCN-related density measurements. For the performance workflow, multiple photographic reference scales can be used (and their contribution to the scaling can be weighed) and scaling can be conducted before the model is build. In this study, the placement of the reference markers in Agisoft Metashape was, however, time-consuming (20-30% of the total expenditure of time per model), and required manual adjustments. Taking advantage of the implemented automatic marker detection in Agisoft Metashape to speed up the scaling did not significantly reduce this time requirement (26% of the total expenditure of time per model for D17-D26). Placing the markers in Agisoft Metashape is, however, optional, as the algorithms implemented in the software are capable of building point clouds without markers. Thus, if no markers are placed and scaling is performed in a similar fashion as in the freeware workflow, the time required to obtain the pit volume can be reduced by approximately one fourth, at the expense of volume accuracy and precision. Furthermore, given the results obtained from the tilted settings and the AT17/18 sampling campaign, the imagery datasets for the pre-dug surface from most settings were too large and could be reduced in order to save both manual and automated processing time. Accordingly, Bauer et al. (2014) and Berney IV et al. (2018) reported having generally taken less than 20 photographs per surface for their photogrammetry-based reconstructions.

The tendency of the calculated volumes to slightly underestimate the reference volume might to a certain extent also be related to the scaling procedure, which was generally performed in a conservative way. A similar pattern was identified by Bauer et al. (2014) for their dataset. However, we also found that the area around the contact zone between board and flowerpot was often slightly dented in the final model, causing a volume reduction. This was most likely due to the low image texture in that area caused by the white and shiny silicone glue used to seal the contact surfaces between flowerpot and board (e.g. James and Robson, 2012).

4.2 Field tests

The generally good agreement between SfM-MVS photogrammetry-based and reference volumes is also valid for the BD17 field tests. However, the applied workflows mostly failed to generate accurate and precise reproductions of the volume of the boulder placed into the pits of BD17-P11.1 and -P12.1. This was mainly due to the lack of sufficient image coverage and significant shading, especially of the parts of the boulder located close to the pit ground. These areas were neglected while taking pictures from different angles as they were mostly concealed by the corners of the pit. A stronger variation in shooting distances and –angles probably would have improved the results (Mosbrucker et al., 2017 and ref. therein). Therefore, the imaging strategy during the AT17/18 fieldwork included close ups of hidden or shaded areas within the respective pits from different angles.

The consistency of values for V_{SfM} at site BD17-P11 can be regarded as an indication, that SfM-MVS photogrammetry reproduced the "true" volume of the pit more accurately than V_{PU}. This finding might be to a certain extent explained by the

way V_{PU} was derived. The casts of the pits BD17-P11 and -P12 were too large to fit into standard 51 L barrels which were used to submerge the casts into water. As a consequence, they were cut into 13 (BD17-P11) and 12 (BD17-P12) parts, which were then submerged one by one (thereby increasing the measurement error). Although we cut the casts carefully, we could not avoid ripping off a high quantity of small globules from the polystyrene blocks that made up most of the inside filling of the casts. This loss in volume could have contributed to the large difference between the photogrammetry-based volumes and the volumes of the casts for site BD17-P11, although the volume of the cast of BD17-P12 matches the SfM-MVS photogrammetry-based volumes quite well. However, an underestimation of the pit volume of site BD17-P11 by V_{PU} is further supported if the final photogrammetry-based densities of sites BD17-P01, -P06 and -P11 are compared. All three pits were dug into the same gravel layer within a radius of < 20 m. Accordingly, the field-state bulk densities are very similar (about 2.08 g cm^{-3} to 2.14 g cm^{-3} when the performance workflow-based volumes are considered; Table 4). These values are further in accordance with the reference densities of BD17-P01 and -P06 (~2.12 g cm^{-3}); only for the reference $\rho_{B,f}$ of BD17-P11, a value of 2.34 ± 0.05 g cm^{-3} is obtained.

The significant difference between the SfM-MVS photogrammetry-based and the densities calculated from the soil sample rings at site BD17-P11 is not surprising as the latter method is not suited to sample such coarse-grained and poorly sorted material (e.g. McLintock, 1959; Muller and Hamilton, 1992). Especially cm-sized clasts cause problems recovering all sample material properly. Thus, material intake during the sampling into the soil sample rings is insufficient and the mass of the sample is underestimated. Furthermore, a continuous sampling from the top to the bottom of the pit's walls was impeded by loose gravels and sands. The high scatter of soil sample ring density data derived from the BD17-P11 site reflects a strong inhomogeneity of the regolith profile, where a ~8 cm thick loess layer covered gravel layers and a ~7 cm thick sand layer (see supplement). The analysis of inhomogeneous soils has been shown to be difficult in terms of accurately measuring bulk densities elsewhere (e.g. Brahim et al., 2012; Manrique and Jones, 1991). This was, however, not the case at sites BD17-P12 and -P13, where the samples were taken from homogenous loess layers. It is likely that compaction, predominantly due to mining traffic and a greater depth below the surface (Manrique and Jones, 1991), caused higher bulk densities at site BD17-P12, which was located on an access ramp. A comparison of the PU foam cast of the cavity dug at site BD17-P13 with the SfM-MVS photogrammetry-based model revealed that the PU foam cast did not include a void at the right outer rim of the cavity. From the picture documentation we realised that this area as well as the lower rim of the cavity were accidentally cut from the PU cast when the latter was removed from the cavity after hardening, a problem already described by Brye et al. (2004). The cutting was necessary because a wooden board used to prevent the foam from expanding outside the cavity did not completely fit the cavity. As a consequence, the foam did ooze between the rim of the board and the rim of the cavity. However, removing these areas also from the DSLM/performance workflow model yields a volume of 4239 ± 70 cm^3 and a field bulk density of 1.52 ± 0.03 g cm^{-3}, which is in good agreement with the reference value of 1.54 ± 0.03 g cm^{-3}. Vice versa, the (original) SfM-MVS photogrammetry-based densities also match the sample ring-based reference densities. Thus, we conclude that the SfM-MVS photogrammetry-based model of BD17-P13 is more accurate than the PU foam-based reference value obtained for $\rho_{B,f}$, underlining the applicability of the method tested in this study in the field even for sites featuring badly illuminated surfaces (the top of the cavity was heavily shadowed, see supplement). Taken together with the results obtained from the tests performed using the artificial pit in a tilted position (Section 3.1), this implies that the method tested here can also be used to estimate densities along sediment depth profiles, where the inherited nuclide concentration, the surface erosion rate and/or the surface age, can be derived from TCN depth sampling (e.g. Braucher et al., 2009). For this kind of analysis, the derivation of sediment densities can be complex (for examples see Brye et al., 2004; Rodríguez-Rodríguez et al., 2020), but the (time-integrated) sediment density accuracy and precision can largely affect the overall results (e.g. Braucher et al., 2009; Hidy et al., 2010; Rodés et al., 2011).

As argued for the tests performed on the artificial pit (Section 4.1), scaling issues are most likely the main cause of slightly less accurate and precise results obtained from the freeware workflow. The results also further indicate that using imagery data

taken with the smartphone camera in JPEG format yields volume reconstructions of similar accuracy as those that are DSLM-based. Thus, there is no need to carry expensive camera equipment in the field if a smartphone is carried that has a camera with comparable hardware properties as the one used in the tests of this study.

540 In contrast to the tests conducted using the artificial pit, the performance workflow required less time to reconstruct a watertight model (see Table B1). Although the non-automated time fraction of the processing is larger than for the freeware workflow, it is more convenient due to the ability of performing batch processing. Furthermore, the non-automated processing in the performance workflow can potentially be significantly reduced, at the expense of accuracy and precision (Section 4.1).

Finally, when compared to the broad range of established methods to determine soil bulk densities, the SfM-MVS

545 photogrammetry-based method as tested in this study regularly yields results of comparable precision and accuracy. Values for measurement precision and/or accuracy as found in the literature are generally about 5% to 15% of the mean bulk density for the clod, core and non-photogrammetry excavation methods in uniform substrates (Casanova et al., 2016; Coelho, 1974; Grossman and Reinsch, 2002 and ref. therein; Muller and Hamilton, 1992; Timm et al., 2005). This holds also for some indirect measurement techniques, such as the TDR method (Liu et al., 2008) and nuclear radiation methods (Timm et al., 2005). In

550 contrast to that, soil bulk densities of gravelly soils derived from uncalibrated pedotransfer functions have been shown to be less accurate (Casanova et al., 2016).

4.3 Aspect-related density contrasts in the Altos de Talinay

The results obtained from the stepwise volume derivation at sites AT17-001, -028, and -029 as well as the comparison of densities of close-by dug pits [AT17-032, -032TS; AT18-102(1), -102(2)] confirm the high precision and accuracy of the SfM-

555 MVS photogrammetry-based soil field bulk densities. In order to scale local TCN production rates for bedrock and/or saprolite covered by soil, $\rho_{B,f}$ seems to be sufficient in the study area, as values for $\rho_{B,d}$ do mostly not differ significantly from the field-state. Given the assumption that the aliquot sample sufficiently mirrors the physical properties of the entire excavation, the inference of $V_{a,r}$ is the most delicate step to approximate ρ_d. The comparably small standard deviation (0.11 g cm^{-3}) from ρ_{BR} measurements indicates that despite some heterogeneities present in the bedrock lithology, it is reasonable to use ρ_{BR} to

560 approximate ρ_d. $V_{a,r}$ could also be measured directly, but this can result in high relative measurement uncertainties in soils with low contents of the > 2 mm fraction if the aliquot sample size is too small (e.g. Soil Survey Staff, 2014; Vincent and Chadwick, 1994). If no reliable estimation of ρ_{BR} can be made, a possible workaround could be to sample a certain amount of the > 2 mm fraction and measure its volume in the laboratory. Vincent and Chadwick (1994) have shown that a representative sample mass to reflect the particle size distribution of a gravelly soil is on the order of ~10 kg, which would then have to be sieved in the

565 field to retain the > 2 mm fraction. However, this implies that at least one additional sieve and the aliquot material would have to be carried along (e.g. 3 kg of gravel from a soil containing 30% gravel by mass).

The tendency towards lower values for $\rho_{B,f}$ (and $\rho_{B,d}$, ρ_d in C1 and C2) and higher values for z on SFS than on NFS might be linked to slope exposure with respect to insolation, causing contrasting microclimatic conditions and thus the observed differences in vegetation cover and presumed differences in soil properties (e.g. Bockheim and Hartemink, 2017; Dal Bo et

570 al., 2019; Gutiérrez-Jurado and Vivoni, 2013b; Jenny, 1994; Pelletier and Swetnam, 2017). We found that the aspect-related contrasts in measured densities are especially pronounced close to the thalwegs. This finding could be related to the steeper slopes, relief-induced increased soil moisture and a greater shielding from solar radiation in this zone, enhancing the differences in microclimatic conditions, vegetation contrasts and associated weathering and erosion processes (Bernhard et al., 2018; Gutiérrez-Jurado and Vivoni, 2013b; Jenny, 1994; Oeser et al., 2018; Fig. 9,10). This assumption could also explain the less

575 pronounced contrasts along the transect in catchment C5, where erosional processes have widened the valley more than at the transects of C1 and C2. We further note that the mean value for $\rho_{B,f}$ on the SFS of C5 is affected by the fact that we could dig only one pit at the lower portion of the slope due to a general inaccessibility and a high abundance of cobbles and boulders (slope debris) in this area.

The mean differences in bulk densities between NFS and SFS are pronounced but not significant, supporting the results of recent studies which did not find significant differences in most present-day physical and chemical properties of regolith on NFS and SFS in the Coastal Cordillera of Northern Chile (Bernhard et al., 2018; Oeser et al., 2018). Measured soil bulk densities and/or soil depths derived from study sites in the semiarid natural reserve of Santa Gracia, located ~120 km NNE of our study area, are very similar to those derived in this study (Bernhard et al., 2018; Dal Bo et al., 2019; Oeser et al., 2018; Owen et al., 2011).

Regarding the quality and expenditure of time to derive the final watertight meshes we did not find significant differences between the two DSLM cameras used. As 30 or less pictures in total were sufficient to generate watertight models accurately reflecting the original pit, both semi-automated marker placement/scaling and automated computing time was likely unnecessarily increased at many sites (e.g. Eltner et al., 2016). The main driver of time consumption for the automatic process steps is the number of pictures that has been taken. Although the computer hardware in use was less powerful than that used during the testing phase, computing times are comparable, emphasizing that also consumer-grade computer hardware is sufficient to generate watertight meshes in reasonable time. However, the placement of markers required the bulk of the expenditure of time. Besides the marker/scaling issues discussed for the tests performed on the artificial pit (the marked photographic reference scales were not used during the BD17 field tests and the field campaign), the alignment of the pre-dug and the pit surfaces were time-consuming. To overcome this problem, we suggest using at least four screw-and-washer assemblies per setting, which can serve as fixed reference points in both the pre-dug and the pit surfaces. Screw-and-washer assemblies are lightweight and do not add a significant amount of baggage to the total baggage to be carried into the field.

5 Conclusion

For several fields of research, including the inferences of process rates and ages based on the quantification of concentrations from TCN, an accurate knowledge of soil bulk densities can be of great importance. We have tested SfM-MVS photogrammetry-based workflows which are suited for non-expert applicants (in photography, the SfM-MVS photogrammetry technique and programming) to measure soil bulk densities that yield results of high accuracy and precision (generally > 95 %), if a proper imaging strategy is applied and a consumer-grade camera is used. Furthermore, watertight models of the excavation from an imagery dataset can be derived without any extra costs, if an up-to-date computer is available. The method is especially suited for fieldwork teams that work in remote areas and whose capability of carrying tools and/or samples are limited by backpack space and work force. If the sampling for TCN requires the excavation of soil, the overall sampling procedure is not significantly being prolonged by weighting the excavated material and taking pictures. If deeper knowledge on soil properties is required or values for $\rho_{B,d}$ and ρ_d should be inferred, an aliquot-size sampling of the soil can yield reasonable approximations in gravelly soils. By applying the method in a study area in the Coastal Cordillera of northern central Chile, we found field-state bulk density values to generally reflect slope aspect, although the differences between NFS and SFS are insignificant. However, significant differences are detectable along diffusively-eroding slope noses within a few tens of metres. This indicates that the determination of a single slope-wide density value for cosmogenic nuclide analysis would be insufficient to accurately characterise surface process rates along the slope.

Data availability

All input files needed to reproduce the modelled volumes are available by the corresponding author upon request.

Author contribution

Conceptualisation by SB, TD and JM. GR and JM designed the artificial pit to test the method. Pictures were taken by GR, KK, CM, and JM. Computer workflows established by GR and JM and applied by KK, GR and JM. NT helped to improve the

computer workflows. Any preparation and analysis of physical samples were performed by CM and JM. The project was supervised by TD. JM wrote the manuscript and SB significantly improved it. All co-authors internally reviewed the manuscript prior to submission.

Competing interests

The authors declare that they have no conflict of interest.

Acknowledgements

We would like to thank the Unternehmensgruppe (consortium) Tholen, Geilenkirchen, Germany, who allowed us to conduct our BD17 field tests on their property and who provided valuable support. Many thanks go also to Leonard Schmidt and Niklas Wehmann, who helped a lot conducting the BD17 field tests and AT18 sampling campaign, respectively. We are grateful to Bill Phillips for helping us tracking down some literature. Moreover, we would like to thank Eduardo Campos and colleagues at the UCN in Antofagasta for their help and support. Damián Lopez helped a lot organising the field work to northern central Chile in 2018. Finally, we thank Ángel Rodés and one anonymous referee for their valuable comments and suggestions on this manuscript. The research was part of a pilot study for a coordinated research centre founded by the Deutsche Forschungsgemeinschaft (DFG, German Research Foundation) – Projektnummer 268236062 – SFB 1211.

Appendix A: List of mathematical symbols

f_d	Conversion factor to approximate the dry mass of an excavation
$f_{r,d}$	Conversion factor to approximate the mass of the > 2 mm fraction of an oven-dried excavation
$f_{r,V}$	Conversion factor to approximate the volume of the > 2 mm fraction of an excavation
$m_{a,f}$	Mass of an aliquot sample in field-state (in grams)
$m_{a,d}$	Mass of an oven-dried aliquot sample (in grams)
$m_{a,r}$	Mass of the fraction > 2 mm in an aliquot sample (in grams)
$m_{e,d}$	Total oven-dried mass of an excavation (in grams)
$m_{e,f}$	Total mass of an excavation in field-state (in grams)
$P(z)$	TCN production rate for a given depth (in atoms per gram and year)
P_0	TCN production rate at the surface (in atoms per gram and year)
V	Volume (in cubic centimetres)
$V_{a,r}$	Volume of the fraction > 2 mm in an aliquot sample (in cubic centimetres)
$V_{b,SfM}$	SfM-MVS photogrammetry-based volume of the boulder used during the field tests in BD17-P11.1 and –P12.1 (in cubic centimetres)
$V_{b,ref}$	Reference volume of the boulder used during the field tests in BD17-P11.1 and –P12.1 (in cubic centimetres)
V_{SfM}	SfM-MVS photogrammetry-based volume of a soil pit (in cubic centimetres)
V_{PU}	Reference volume of a soil pit based on PU foam casts (in cubic centimetres)
z	Soil depth (in centimetres)
Λ	Attenuation path length of cosmic rays (in grams per square centimetre)
ρ	Density (in grams per cubic centimetre)
ρ_B	Soil bulk density (in grams per cubic centimetre)
$\rho_{B,d}$	Dry soil bulk density (in grams per cubic centimetre)

$\rho_{B,f}$	Field-state soil bulk density (in grams per cubic centimetre)
ρ_{BR}	Bedrock density (in grams per cubic centimetre)
ρ_d	Dry soil density (in grams per cubic centimetre)
ρ_{H2O}	Density of water (in grams per cubic centimetre)

665

Appendix B: Tables

References

Al-Shammary, A. A. G., Kouzani, A. Z., Kaynak, A., Khoo, S. Y., Norton, M., and Gates, W.: Soil Bulk Density Estimation Methods: A Review, Pedosphere, 28, 581-596, 2018.

670 Armesto, J. J. and Martínez, J. A.: Relations Between Vegetation Structure and Slope Aspect in the Mediterranean Region of Chile, Journal of Ecology, 66, 881-889, 1978.

Balco, G.: Production rate calculations for cosmic-ray-muon-produced 10Be and 26Al benchmarked against geological calibration data, Quaternary Geochronology, 39, 150-173, 2017.

Bauer, T., Strauss, P., and Murer, E.: A photogrammetric method for calculating soil bulk density, Journal of Plant Nutrition and Soil Science,
675 177, 496-499, 2014.

Berney IV, E., Ganesh, N. B., and Pratt, T. C.: A Photogrammetric Method for Obtaining Soil Density, U.S. Army Engineer Research and Development Center, Vicksburg, 2018.

Bernhard, N., Moskwa, L.-M., Schmidt, K., Oeser, R. A., Aburto, F., Bader, M. Y., Baumann, K., von Blanckenburg, F., Boy, J., van den Brink, L., Brucker, E., Büdel, B., Canessa, R., Dippold, M. A., Ehlers, T. A., Fuentes, J. P., Godoy, R., Jung, P., Karsten, U., Köster, M.,
680 Kuzyakov, Y., Leinweber, P., Neidhardt, H., Matus, F., Mueller, C. W., Oelmann, Y., Oses, R., Osses, P., Paulino, L., Samolov, E., Schaller, M., Schmid, M., Spielvogel, S., Spohn, M., Stock, S., Stroncik, N., Tielbörger, K., Übernickel, K., Scholten, T., Seguel, O., Wagner, D., and Kühn, P.: Pedogenic and microbial interrelations to regional climate and local topography: New insights from a climate gradient (arid to humid) along the Coastal Cordillera of Chile, CATENA, 170, 335-355, 2018.

Blake, G. R. and Hartge, K. H.: Bulk Density. In: Methods of Soil Analysis: Part 1—Physical and Mineralogical Methods, Klute, A. (Ed.),
685 SSSA Book Series, 5.1, Soil Science Society of America, American Society of Agronomy, Madison, WI, 1986.

Bockheim, J. G. and Hartemink, A. E.: Soil-forming factors. In: The soils of wisconsin, Springer, 2017.

Borchers, B., Marrero, S., Balco, G., Caffee, M., Goehring, B., Lifton, N., Nishiizumi, K., Phillips, F., Schaefer, J., and Stone, J.: Geological calibration of spallation production rates in the CRONUS-Earth project, Quaternary Geochronology, 31, 188-198, 2016.

Brahim, N., Bernoux, M., and Gallali, T.: Pedotransfer functions to estimate soil bulk density for Northern Africa: Tunisia case, Journal of
690 Arid Environments, 81, 77-83, 2012.

Braucher, R., Del Castillo, P., Siame, L., Hidy, A. J., and Bourlés, D. L.: Determination of both exposure time and denudation rate from an in situ-produced 10Be depth profile: A mathematical proof of uniqueness. Model sensitivity and applications to natural cases, Quaternary Geochronology, 4, 56-67, 2009.

Brye, K. R., Morris, T. L., Miller, D. M., Formica, S. J., and Van Eps, M. A.: Estimating Bulk Density in Vertically Exposed Stoney Alluvium
695 Using a Modified Excavation Method, Journal of Environmental Quality, 33, 1937-1942, 2004.

Casanova, M., Salazar, O., Seguel, O., and Luzio, W.: The Soils of Chile, Springer, 2013.

Casanova, M., Tapia, E., Seguel, O., and Salazar, O.: Direct measurement and prediction of bulk density on alluvial soils of central Chile, Chilean journal of agricultural research, 76, 105-113, 2016.

Coelho, M. A.: Spatial variability of water related soil physical properties. The University of Arizona., 1974.

700 Dal Bo, I., Klotzsche, A., Schaller, M., Ehlers, T. A., Kaufmann, M. S., Fuentes Espoz, J. P., Vereecken, H., and van der Kruk, J.: Geophysical imaging of regolith in landscapes along a climate and vegetation gradient in the Chilean coastal cordillera, CATENA, 180, 146-159, 2019.

Dunai, T. J.: Cosmogenic nuclides : principles, concepts and applications in the earth surface sciences, Cambridge University Press, Cambridge, UK ; New York, 2010.

705 Eltner, A., Kaiser, A., Castillo, C., Rock, G., Neugirg, F., and Abellán, A.: Image-based surface reconstruction in geomorphometry-merits, limits and developments, Earth Surface Dynamics, 4, 2016.

Emparan, C. and Pineda, G.: Geología del Área Andacollo-Puerto Aldea, Región de Coquimbo, Carta Geológica de Chile, Serie Geológica Básica, 2006. 2006.

Fuhrmann, S., Langguth, F., and Goesele, M.: Mve-a multi-view reconstruction environment, 2014, 11-18.

710 Furukawa, Y. and Ponce, J.: Accurate, dense, and robust multiview stereopsis, IEEE transactions on pattern analysis and machine intelligence, 32, 1362-1376, 2009.

Gana, F.: Mapa geológico de la cordillera de la costa entre La Serena y Quebrada El Teniente: Región de Coquimbo, 1991. 1991.

Grossman, R. B. and Reinsch, T. G.: Bulk density and linear extensibility. In: Methods of Soil Analysis: Part 4 Physical Methods, Dane, J. M. and Topp, G. C. (Eds.), methodsofsoilan4, Soil Science Society of America, Madison, Wisconsin, USA, 2002.

715 Gruen, A.: Development and Status of Image Matching in Photogrammetry, The Photogrammetric Record, 27, 36-57, 2012.

Gutiérrez-Jurado, H. A. and Vivoni, E. R.: Ecogeomorphic expressions of an aspect-controlled semiarid basin: I. Topographic analyses with high-resolution data sets, Ecohydrology, 6, 8-23, 2013a.

Gutiérrez-Jurado, H. A. and Vivoni, E. R.: Ecogeomorphic expressions of an aspect-controlled semiarid basin: II. Topographic and vegetation controls on solar irradiance, Ecohydrology, 6, 24-37, 2013b.

720 Gutierrez, J. R., Meserve, P. L., Kelt, D. A., Engilis Jr, A., and Andrea, M.: Long-term research in Bosque Fray Jorge National Park: Twenty years studying the role of biotic and abiotic factors in a Chilean semiarid scrubland, Revista Chilena de Historia Natural, 83, 69-98, 2010.

Hao, X., Ball, B. C., Culley, J. L. B., Carter, M. R., and Parkin, G. W.: Soil density and porosity. In: Soil sampling and methods of analysis, Carter M. R. and Gregorich, E. G. (Eds.), CRC Press, 2008.

Hartel, P. G.: MICROBIAL PROCESSES | Environmental Factors. In: Encyclopedia of Soils in the Environment, Hillel, D. (Ed.), Elsevier, Oxford, 2005.

Heimsath, A. and Jungers, M.: Processes, transport, deposition, and landforms: quantifying creep. In: Treatise on Geomorphology, Elsevier Inc., 2013.

Heimsath, A. M. and Burke, B. C.: The impact of local geochemical variability on quantifying hillslope soil production and chemical weathering, Geomorphology, 200, 75-88, 2013.

Heimsath, A. M., Dietrich, W. E., Nishiizumi, K., and Finkel, R. C.: The soil production function and landscape equilibrium, Nature, 388, 358-361, 1997.

Hidy, A. J., Gosse, J. C., Pederson, J. L., Mattern, J. P., and Finkel, R. C.: A geologically constrained Monte Carlo approach to modeling exposure ages from profiles of cosmogenic nuclides: An example from Lees Ferry, Arizona, Geochemistry, Geophysics, Geosystems, 11, 2010.

Hippe, K.: Constraining processes of landscape change with combined in situ cosmogenic 14C-10Be analysis, Quaternary Science Reviews, 173, 1-19, 2017.

James, M. R. and Robson, S.: Straightforward reconstruction of 3D surfaces and topography with a camera: Accuracy and geoscience application, Journal of Geophysical Research: Earth Surface, 117, 2012.

Jenny, H.: Factors of soil formation: a system of quantitative pedology, Courier Corporation, 1994.

Kazhdan, M., Bolitho, M., and Hoppe, H.: Poisson surface reconstruction, 2006.

Kazhdan, M. and Hoppe, H.: Screened poisson surface reconstruction, ACM Transactions on Graphics (ToG), 32, 1-13, 2013.

Kels, H.: Bau und Bilanzierung der Lössdecke am westlichen Niederrhein, 2007.PhD thesis, 2007.

Lal, D.: Cosmic ray labeling of erosion surfaces: in situ nuclide production rates and erosion models, Earth and Planetary Science Letters, 104, 424-439, 1991.

Lal, D. and Arnold, J. R.: Tracing quartz through the environment, Proceedings of the Indian Academy of Sciences - Earth and Planetary Sciences, 94, 1-5, 1985.

Lifton, N., Sato, T., and Dunai, T. J.: Scaling in situ cosmogenic nuclide production rates using analytical approximations to atmospheric cosmic-ray fluxes, Earth and Planetary Science Letters, 386, 149-160, 2014.

Liu, X., Ren, T., and Horton, R.: Determination of soil bulk density with thermo-time domain reflectometry sensors, Soil Science Society of America Journal, 72, 1000-1005, 2008.

López-Cortés, F. and López, D.: Antecedentes bioclimáticos del parque nacional bosque fray jorge, Historia Natural del Parque Nacional Bosque Fray Jorge, 2, 45-60, 2004.

Manrique, L. A. and Jones, C. A.: Bulk Density of Soils in Relation to Soil Physical and Chemical Properties, Soil Science Society of America Journal, 55, 476-481, 1991.

Maynard, D. G. and Curran, M. P.: Bulk density measurement in forest soils. In: Soil sampling and methods of analysis, Carter M. R. and Gregorich, E. G. (Eds.), CRC Press, 2008.

McLintock, T. F.: A Method for Obtaining Soil-Sample Volumes in Stony Soils, Journal of Forestry, 57, 832-834, 1959.

Micheletti, N., Chandler, J. H., and Lane, S. N.: Investigating the geomorphological potential of freely available and accessible structure-from-motion photogrammetry using a smartphone, Earth Surface Processes and Landforms, 40, 473-486, 2015.

Mosbrucker, A. R., Major, J. J., Spicer, K. R., and Pitlick, J.: Camera system considerations for geomorphic applications of SfM photogrammetry, Earth Surface Processes and Landforms, 42, 969-986, 2017.

Mosbrucker, A. R., Spicer, K. R., Christianson, T. S., and Uhrich, M. A.: Estimating concentrations of fine-grained and total suspended sediment from close-range remote sensing imagery, 2015.

Muller, R. N. and Hamilton, M. E.: A simple, effective method for determining the bulk density of stony soils, Communications in Soil Science and Plant Analysis, 23, 313-319, 1992.

Neale, W. T., Hessel, D., and Terpstra, T.: Photogrammetric Measurement Error Associated with Lens Distortion, 2011.

Nishiizumi, K., Lal, D., Klein, J., Middleton, R., and Arnold, J. R.: Production of 10Be and 26Al by cosmic rays in terrestrial quartz in situ and implications for erosion rates, Nature, 319, 134, 1986.

Oeser, R. A., Stroncik, N., Moskwa, L.-M., Bernhard, N., Schaller, M., Canessa, R., van den Brink, L., Köster, M., Brucker, E., Stock, S., Fuentes, J. P., Godoy, R., Matus, F. J., Oses Pedraza, R., Osses McIntyre, P., Paulino, L., Seguel, O., Bader, M. Y., Boy, J., Dippold, M. A., Ehlers, T. A., Kühn, P., Kuzyakov, Y., Leinweber, P., Scholten, T., Spielvogel, S., Spohn, M., Übernickel, K., Tielbörger, K., Wagner, D., and von Blanckenburg, F.: Chemistry and microbiology of the Critical Zone along a steep climate and vegetation gradient in the Chilean Coastal Cordillera, CATENA, 170, 183-203, 2018.

Owen, J. J., Amundson, R., Dietrich, W. E., Nishiizumi, K., Sutter, B., and Chong, G.: The sensitivity of hillslope bedrock erosion to precipitation, Earth Surface Processes and Landforms, 36, 117-135, 2011.

Page-Dumroese, D. S., Brown, R. E., Jurgensen, M. F., and Mroz, G. D.: Comparison of Methods for Determining Bulk Densities of Rocky Forest Soils, Soil Science Society of America Journal, 63, 379-383, 1999.

Pelletier, J. D. and Swetnam, T. L.: Asymmetry of weathering-limited hillslopes: the importance of diurnal covariation in solar insolation and temperature, Earth Surface Processes and Landforms, 42, 1408-1418, 2017.

Phillips, F. M., Argento, D. C., Balco, G., Caffee, M. W., Clem, J., Dunai, T. J., Finkel, R., Goehring, B., Gosse, J. C., Hudson, A. M., Jull, A. J. T., Kelly, M. A., Kurz, M., Lal, D., Lifton, N., Marrero, S. M., Nishiizumi, K., Reedy, R. C., Schaefer, J., Stone, J. O. H., Swanson, T., and Zreda, M. G.: The CRONUS-Earth Project: A synthesis, Quaternary Geochronology, 31, 119-154, 2016.

Rodés, Á. and Evans, D. L.: Cosmogenic soil production rate calculator, MethodsX, 7, 100753, 2020.

Rodés, Á., Pallàs, R., Braucher, R., Moreno, X., Masana, E., and Bourlés, D. L.: Effect of density uncertainties in cosmogenic 10Be depth-profiles: Dating a cemented Pleistocene alluvial fan (Carboneras Fault, SE Iberia), Quaternary Geochronology, 6, 186-194, 2011.

Rodríguez-Rodríguez, L., Antón, L., Rodés, Á., Pallàs, R., García-Castellanos, D., Jiménez-Munt, I., Struth, L., Leanni, L., Aumaître, G., Bourlès, D., and Keddadouche, K.: Dates and rates of endo-exorheic drainage development: Insights from fluvial terraces (Duero River, Iberian Peninsula), Global and Planetary Change, 193, 103271, 2020.

Russo, D.: Leaching Characteristics of a Stony Desert Soil, Soil Science Society of America Journal, 47, 431-438, 1983.

Schaetzl, R. J. and Thompson, M. L.: Soils, Cambridge university press, 2015.

Smith, M., Carrivick, J., and Quincey, D.: Structure from motion photogrammetry in physical geography, Progress in Physical Geography, 40, 247-275, 2016.

Soil Survey Staff: Kellogg Soil Survey Laboratory Methods Manual, U.S. Department of Agriculture, Natural Resources Conservation Service, 2014.

795 Thoeni, K., Giacomini, A., Murtagh, R., and Kniest, E.: A comparison of multi-view 3D reconstruction of a rock wall using several cameras and a laser scanner, The International Archives of Photogrammetry, Remote Sensing and Spatial Information Sciences, 40, 573, 2014.

Timm, L. C., Pires, L. F., Reichardt, K., Roveratti, R., Oliveira, J. C. M., and Bacchi, O. O. S.: Soil bulk density evaluation by conventional and nuclear methods, Soil Research, 43, 97-103, 2005.

Vincent, K. R. and Chadwick, O. A.: Synthesizing Bulk Density for Soils with Abundant Rock Fragments, Soil Science Society of America
800 Journal, 58, 455-464, 1994.

Westoby, M. J., Brasington, J., Glasser, N. F., Hambrey, M. J., and Reynolds, J. M.: 'Structure-from-Motion' photogrammetry: A low-cost, effective tool for geoscience applications, Geomorphology, 179, 300-314, 2012.

805

810

815

820

825
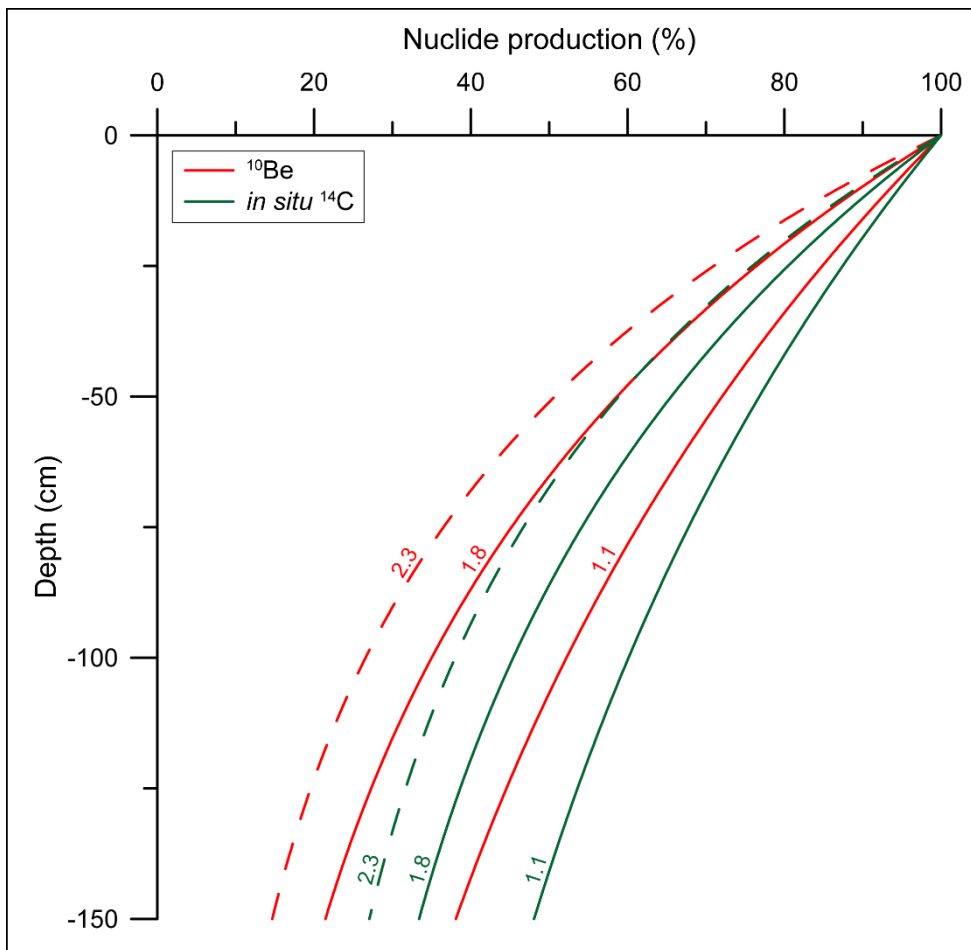
Figure 1. Depth and density dependence of nuclide production (non-eroding surfaces) within homogenous material. Solid lines represent two endmember densities (1.1 g cm^{-3} and 1.8 g cm^{-3}; e.g. Hartel, 2005; Manrique and Jones, 1991; Schaetzl and Thompson, 2015) of typical soils (red: [10]Be; green: *in situ* [14]C). Dashed lines reflect nuclide production for highly compacted soils (2.3 g cm^{-3}; Schaetzl and Thompson, 2015). Calculated for SLHL using the LSDn (Sa) scaling scheme (Lifton et al., 2014) with a spallogenic production rate of 3.92 ± 0.31 at g[-1] for [10]Be and 12.76 ± 0.00 at g[-1] for [14]C (Borchers et al., 2016; Phillips et al., 2016) and including the contribution of muogenic production as implemented in the MATLAB code provided by Balco (2017).
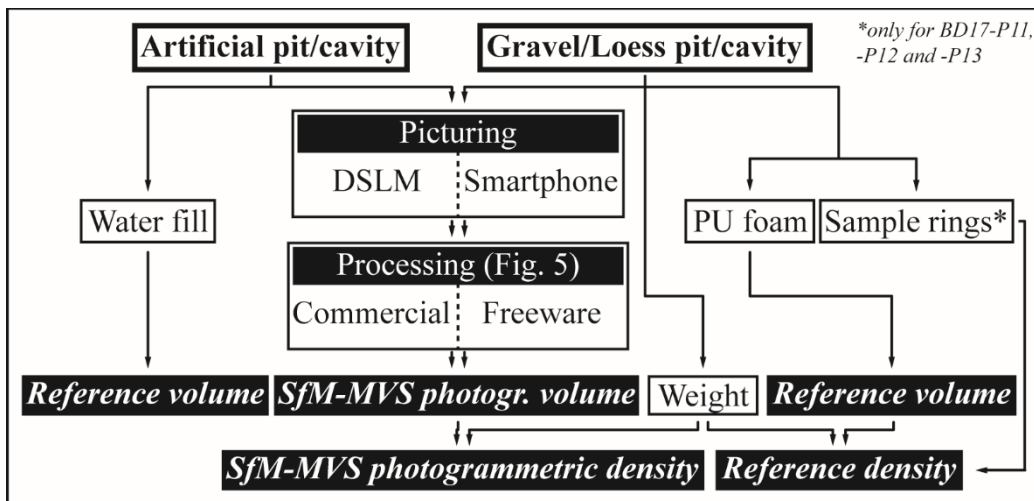
Figure 2. Generalised workflow applied to obtain SfM-MVS photogrammetry-based volumes, reference volumes, and field-state soil bulk densities for testing purposes.
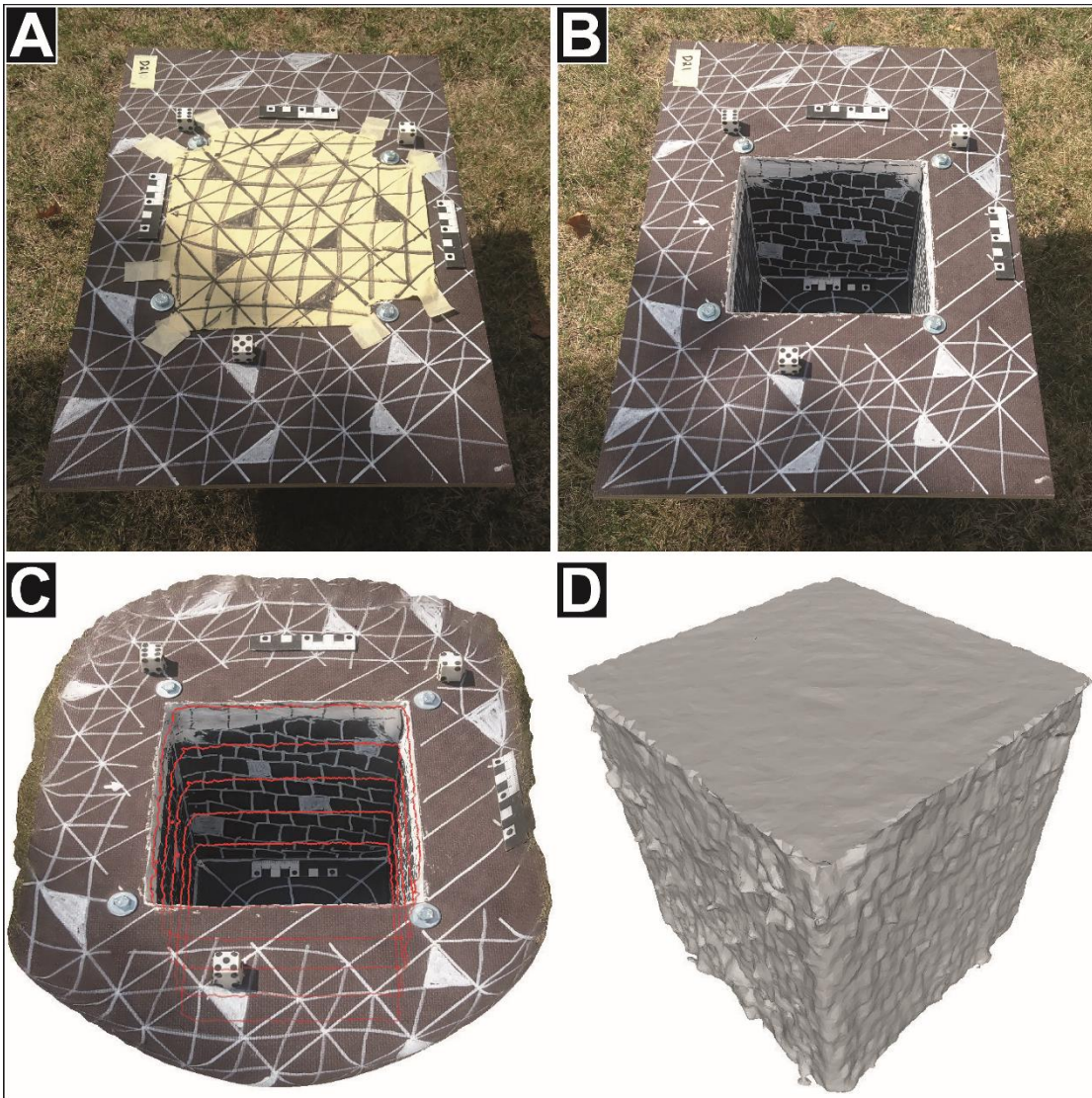
840   Figure 3. The flowerpot with a board attached (D21) with (A) and without (B) the thin fabric covering the opening. The reconstructed artificial pit is shown with 5 cm contours in red (C). To obtain the final watertight mesh, the reconstructions of simulated pre-dug surface and soil pit were merged by bridging the edges of the two meshes (D).
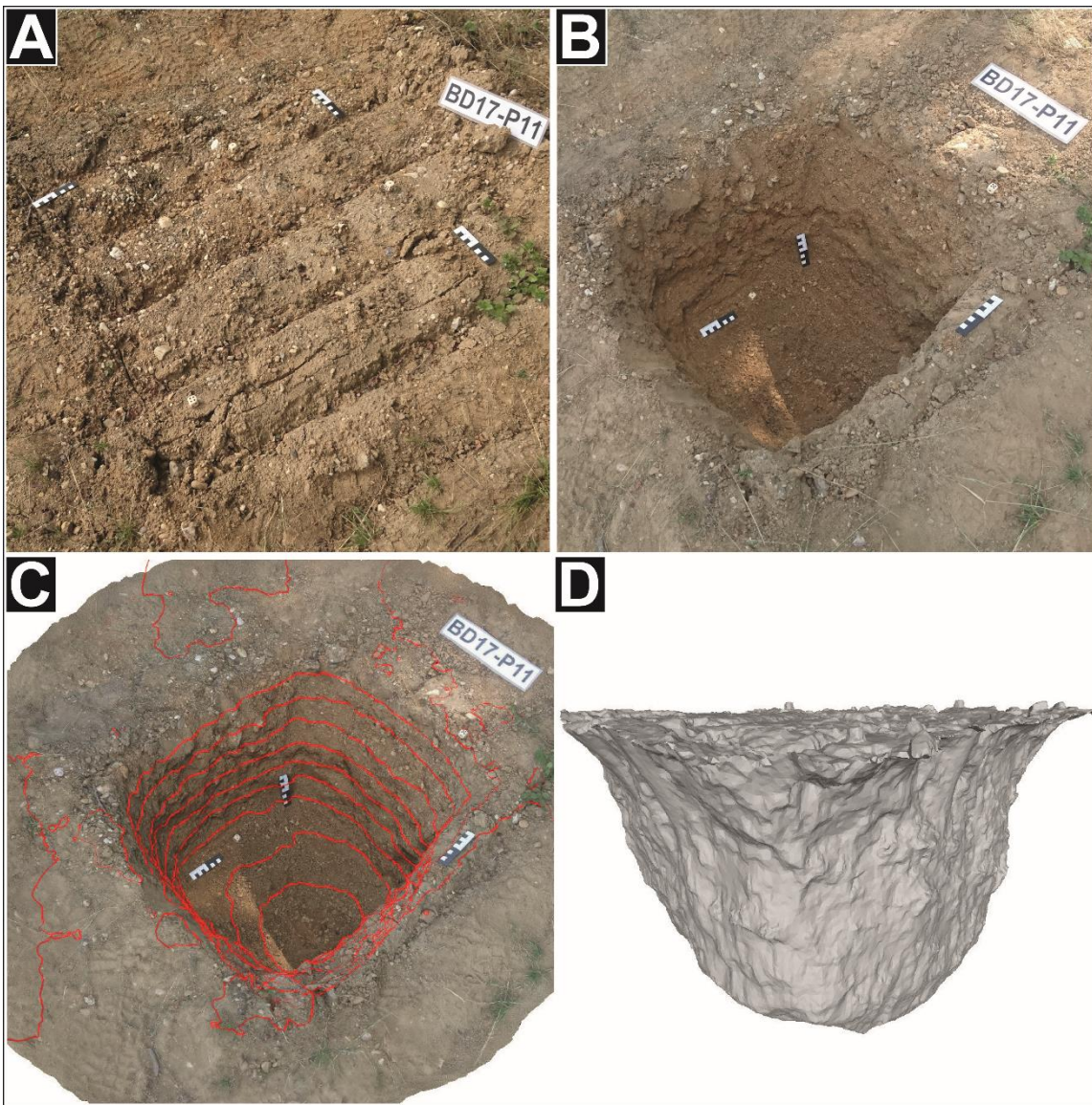
845 **Figure 4. Test site BD17-P11. The pit was dug into gravels situated in a sandy/silty matrix (A, B). The reconstructed pit is shown with 5 cm contours in red (C). The large grain sizes dominating the substrate in which the pit was dug into are reflected by the high surface roughness of the final watertight mesh (D).**
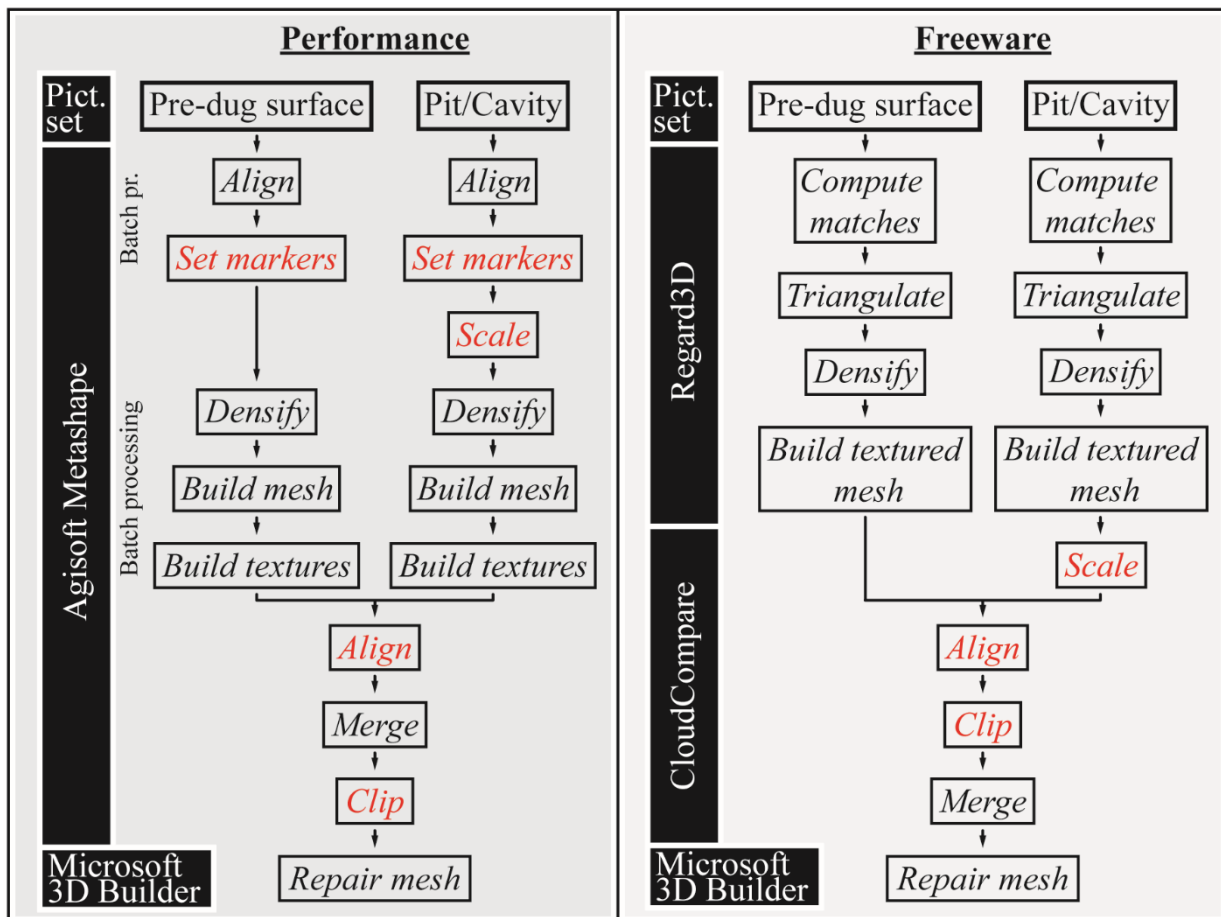
850 **Figure 5. Performance and freeware workflows as applied in this study and the computer programs used. Non- or semi-automated steps are shown in red colour.**
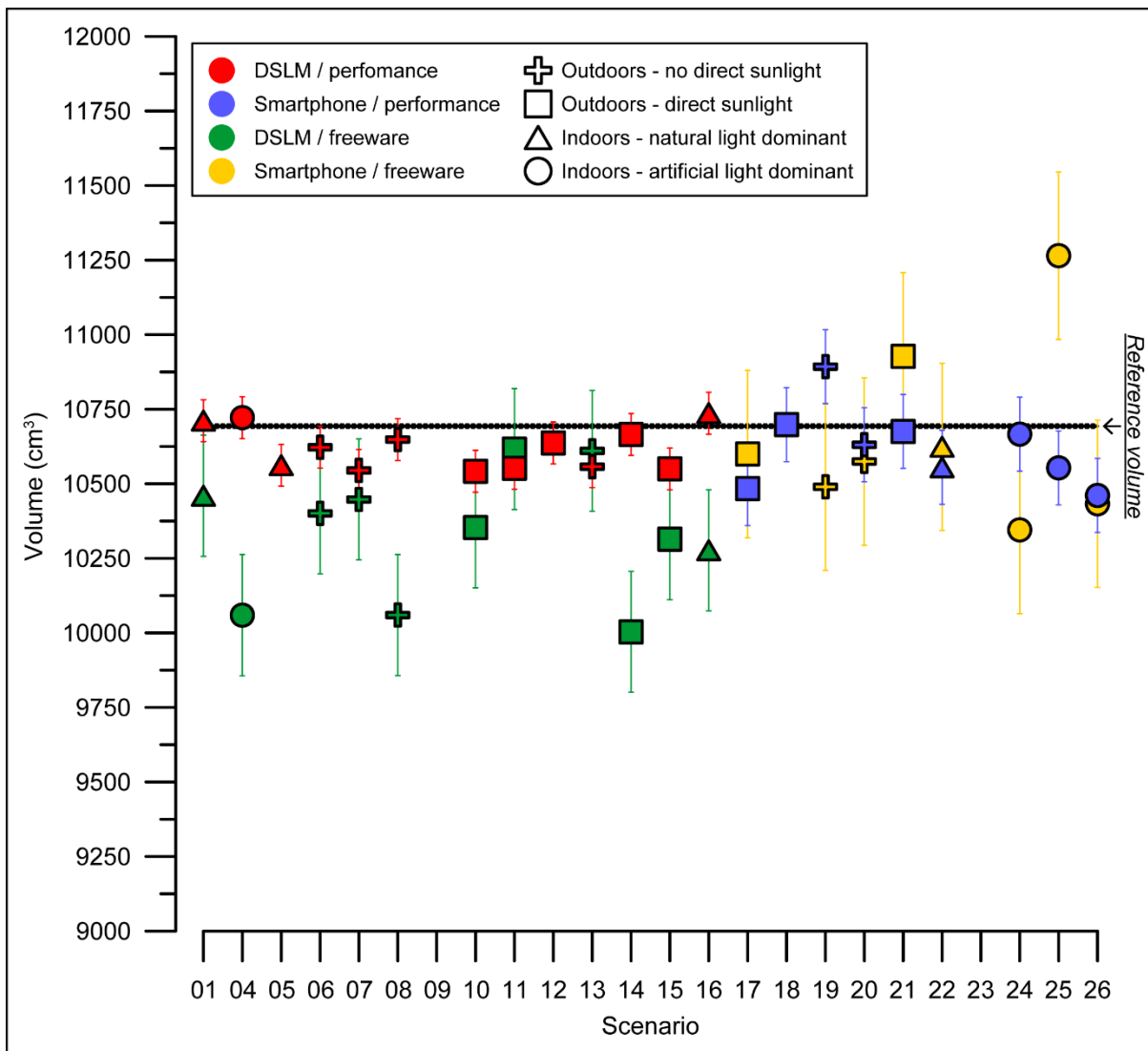
Figure 6. Performance and freeware workflow-derived SfM-MVS photogrammetric volumes of the artificial pit using a DSLM and a smartphone camera for different settings and lighting conditions. The reference volume (solid black line with dashed black error range) of 10693 ± 7 cm³ was measured by filling the empty flowerpot with water and recording the difference in weight (assuming ρ_{H2O} = 1 g cm⁻³ for demineralised water at ~20°C water temperature).
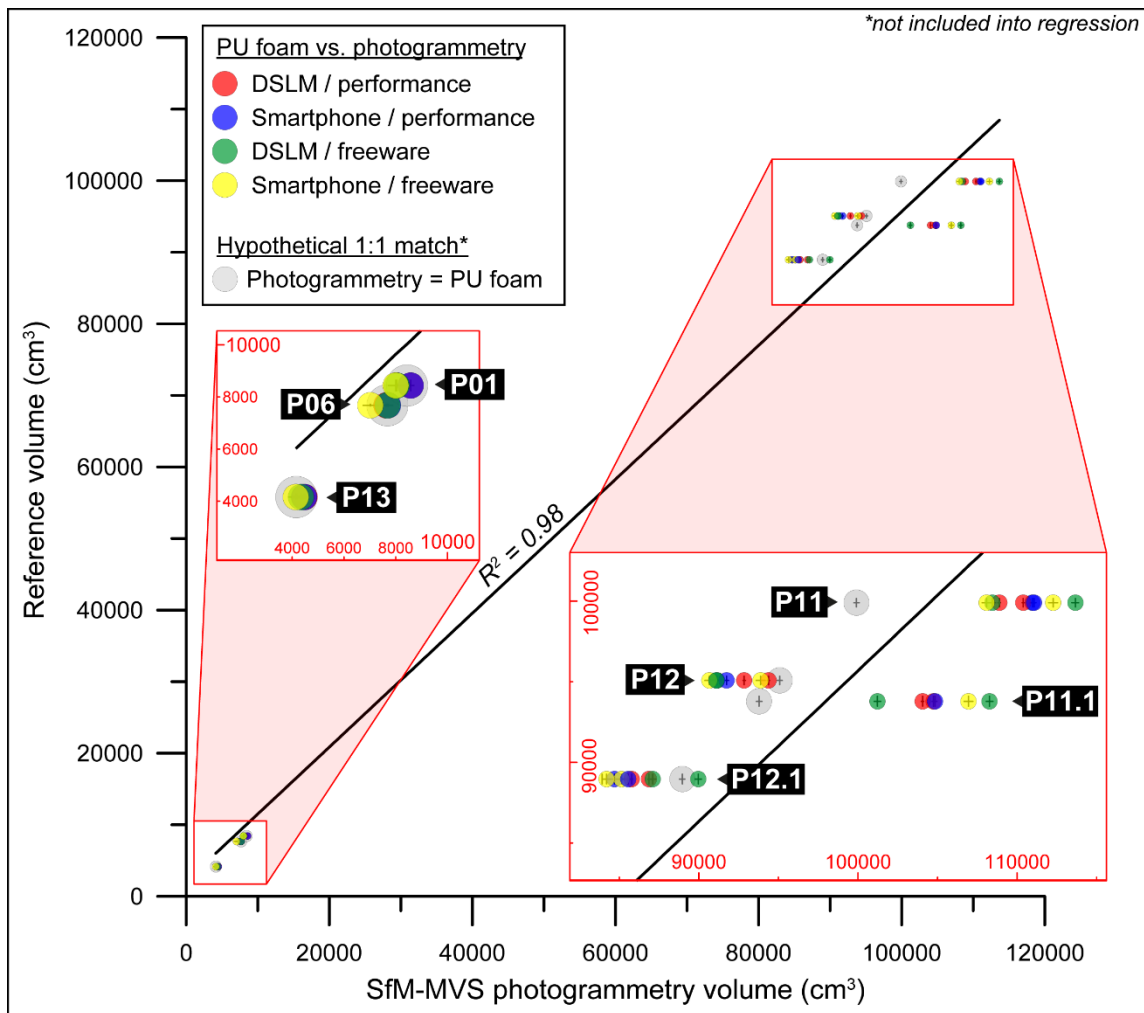
Figure 7. Pit (BD17-P01 to -P12.1) and cavity (BD17-P13) volumes derived using PU foam/polystyrene casts (reference volumes) and the SfM-MVS photogrammetry workflows tested in this study. Hypothetically matching values obtained from the PU foam/polystyrene casts are indicated by large grey circles (errors of these values on the ordinate reflect measurement standard deviations; errors on the abscissa reflect the standard deviation of all photogrammetric reconstructions as determined on the artificial pit, i.e. ~169 cm^3; Table 2). For discussion, see text.
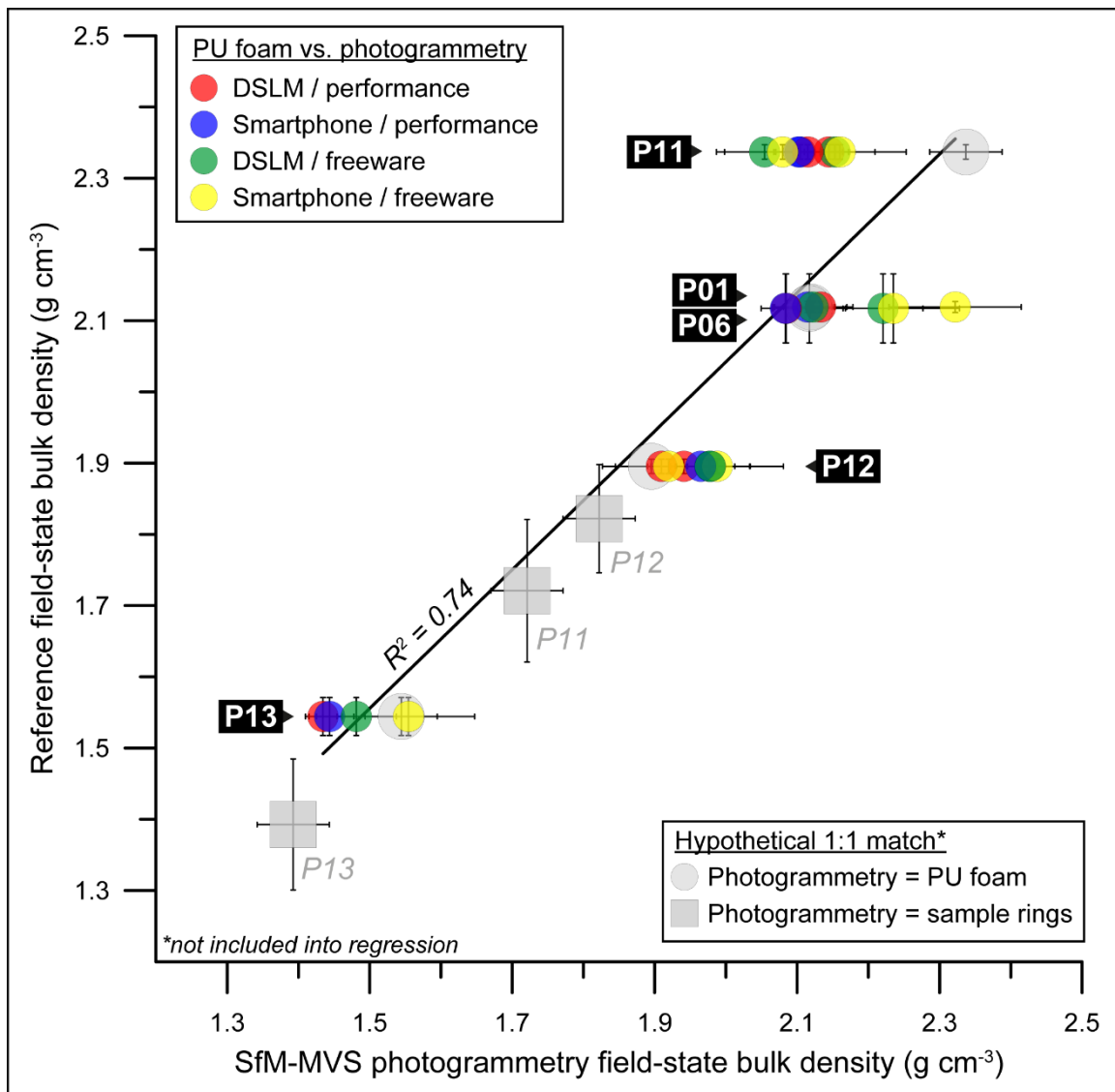
Figure 8. Pit (BD17-P01 to -P12) and cavity (BD17-P13) densities derived using PU foam/polystyrene casts (reference densities) and the photogrammetry workflows presented in this study. Hypothetically matching values obtained from the PU foam/polystyrene casts and soil sample rings are indicated by large grey circles and squares (errors on the ordinate reflect measurement standard deviations; errors on the abscissa reflect the standard deviation of all photogrammetry-based densities for the respective sites). For discussion, see text.

870
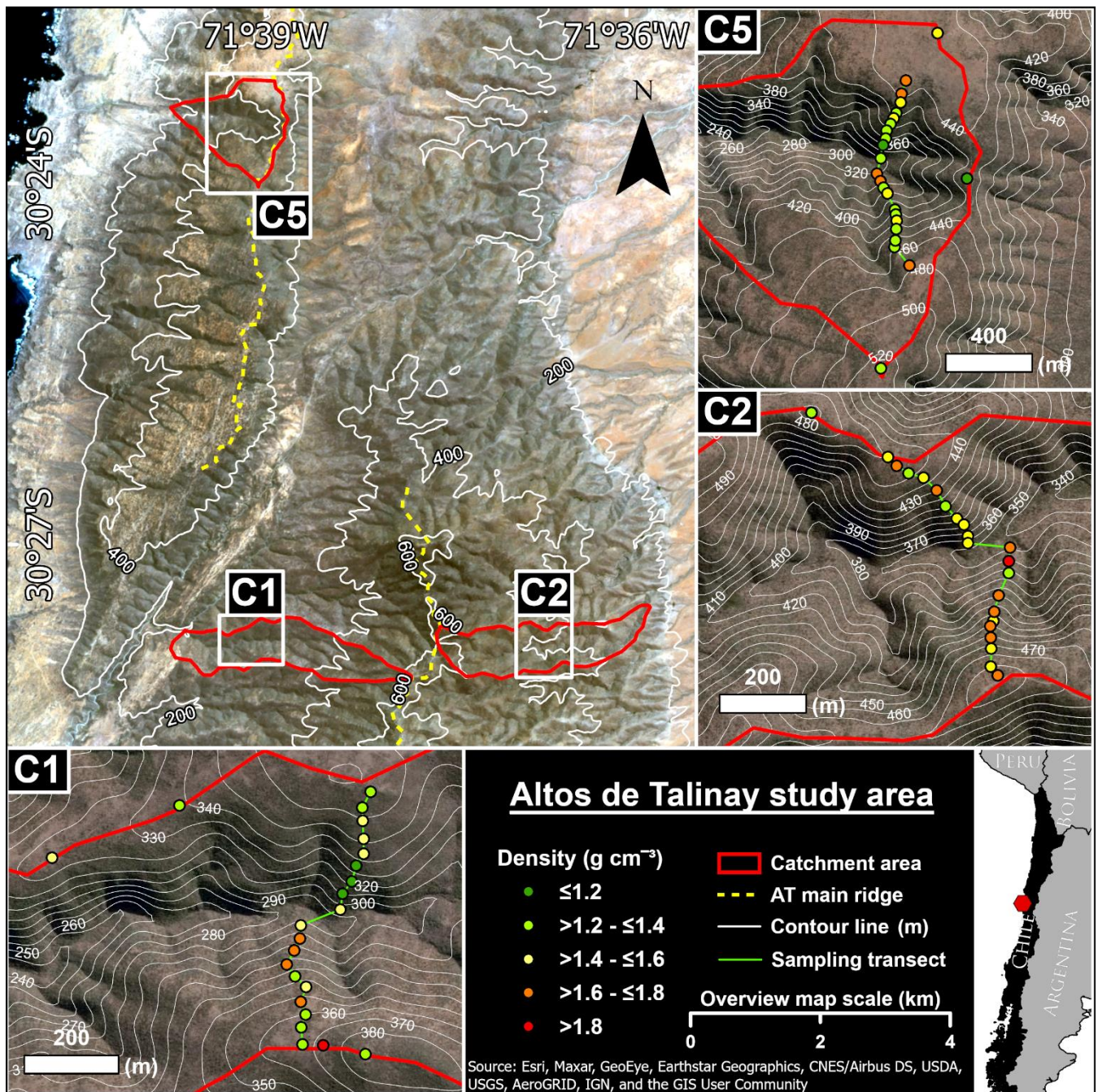
Figure 9. Sentinel 2B satellite image showing the location of AT17/18 study area (overview map). Zoomed inlets show sampling transects and field-state soil bulk densities calculated from SfM-MVS photogrammetry-based volume derivations and in-field excavation mass weighting (satellite image source: ArcGIS World Imagery).
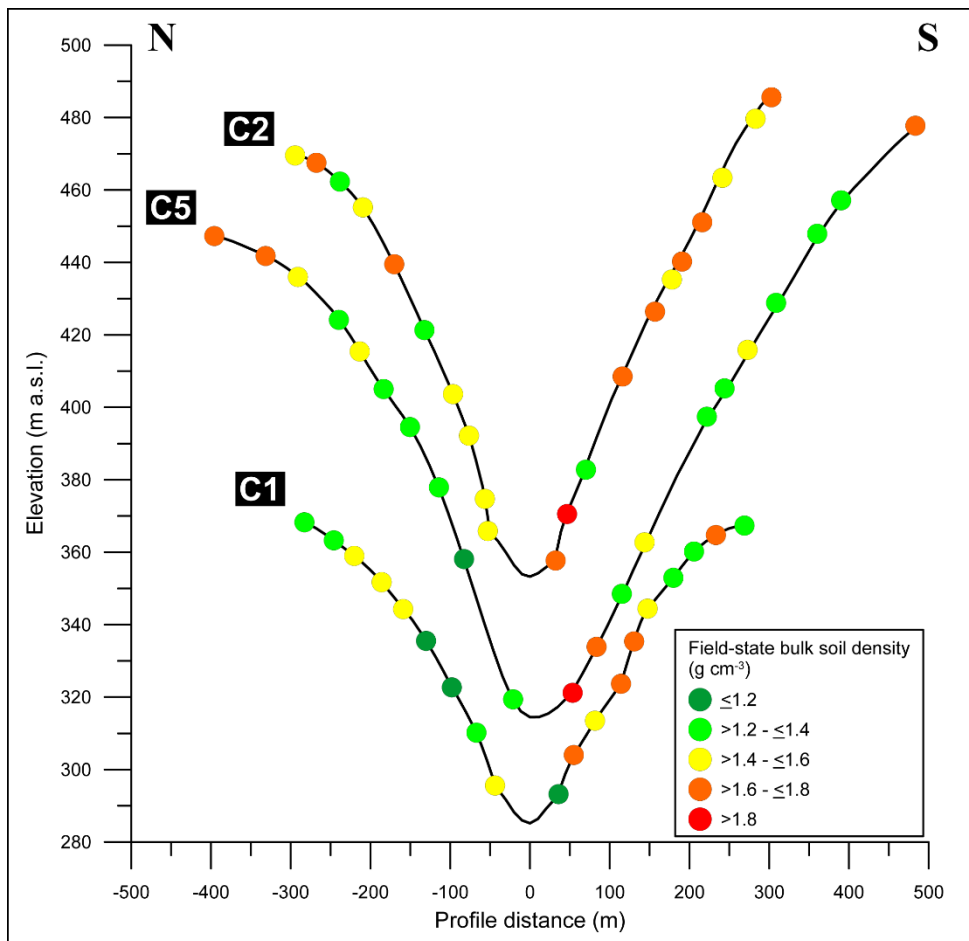
880 **Figure 10. TanDEM-X WorldDEM DTM-derived profiles of AT17/18 sampling transects and field-state soil bulk densities calculated from SfM-MVS photogrammetry-based volume derivations and in-field excavation mass weighing. NFS generally tend to show greater values for $\rho_{B,f}$ than their south-facing counterparts. Contrasts are pronounced in the downslope areas close to the thalwegs.**

Table 1. Test pit designs used for the imaging testing scenarios.

ID	Width (cm)	Length (cm)	Depth b.s. (cm)[a]	Pre-dug surface dip (°)	Pit sidewall material
D01-D26	22	22	23	0-90	PE[b]/silicone
BD17-P01	20	20	25	< 3	Gms[c]
BD17-P06	20	20	25	13	Gms[c]
BD17-P11	60	60	50	< 3	Gms[c]
BD17-P12	60	60	50	12	Loess
BD17-P13	40	15	15	90	Loess

885 **[a] Below pre-dug surface.**

[b] Polyethylene (PE).

[c] Matrix-supported gravel.

890

Table 2: Scenario details and derived volumes (V_{SfM}) of the artificial pit by applying the performance and freeware workflows.

	ID	Lighting[a]	Orientation	Performance V_{SfM} (cm³)	Dif.[b] (%)	Freeware V_{SfM} (cm³)	Dif.[b] (%)
DSLM	D01	3	Horizontal	10711	+0.2	10459	-2.2
	D04	3	Cavity	10721	+0.3	10059	-5.9
	D05	3	Cavity	10562	-1.2	-	-
	D06	1	Tilted	10622	-0.7	10401	-2.7
	D07	1	Horizontal	10544	-1.4	10447	-2.3
	D08	1	Horizontal	10648	-0.4	10059	-5.9
	D09	1	Horizontal	-	-	-	-
	D10	2	Cavity	10542	-1.4	10353	-3.2
	D11	2	Cavity	10552	-1.3	10616	-0.7
	D12	2	Tilted	10637	-0.5	-	-
	D13	1	Horizontal	10557	-1.3	10610	-0.8
	D14	2	Horizontal	10665	-0.3	10003	-6.5
	D15	2	Horizontal	10549	-1.3	10314	-3.5
	D16	3	Horizontal	10736	+0.4	10277	-3.9
			Mean	*10619 ± 70*	*-0.7*	*10327 ± 203*	*-3.4*
Smartphone	D17	2	Horizontal	10483	-2.0	10599	-0.9
	D18	2	Tilted	10698	+0.0	-	-
	D19	1	Cavity	10892	+1.9	10489	-1.9
	D20	1	Horizontal	10630	-0.6	10575	-1.1
	D21	2	Horizontal	10675	-0.2	10927	+2.2
	D22	3	Horizontal	10555	-1.3	10624	-0.6
	D23	4	Cavity	-	-	-	-
	D24	4	Cavity	10666	-0.3	10345	-3.3
	D25	4	Horizontal	10553	-1.3	11265	+5.3
	D26	4	Horizontal	10461	-2.2	10432	-2.4
			Mean	*10624 ± 124*	*-0.6*	*10657 ± 281*	*-0.3*
			Total mean	*10621 ± 96*	*-0.7*	*10466 ± 289*	*-2.1*

[a] Lighting conditions as follows: 1 – outdoors, little or no direct sunlight (i.e. shadowed or cloudy); 2 – outdoors, direct sunlight; 3 – indoors, sunlight as the main illumination source; 4 – indoors, artificial light (ceiling lighting) as the main illumination source.

[b] Difference between the modelled volume and the reference volume (10693 ± 7 cm³).

Table 3. Reference volumes (V_{PU}), excavation masses (field state – $m_{e,f}$; dry – $m_{e,d}$) and densities (field state – $\rho_{B,f}$; dry – $\rho_{B,d}$) obtained from BD17 the test sites.

ID	Reference	V_{PU} (cm³)	$m_{e,f}$ (g)	$m_{e,d}$ (g)	$\rho_{B,f}$ (g cm⁻³)	$\rho_{B,d}$ (g cm⁻³)
P01	PU foam	7683 ± 28	16282 ± 2	15686 ± 2	2.12 ± 0.01	2.04 ± 0.01
P06	PU foam	8441 ± 193	17872 ± 2	17585 ± 1	2.12 ± 0.05	2.08 ± 0.05
P11	PU foam	99905 ± 257	233489 ± 830	-	2.34 ± 0.01	-
	Sample rings[a]	-	-	-	1.72 ± 0.10	1.60 ± 0.09
P11.1	PU foam/boulder[b]	93789 ± 326	-	-	-	-
P12	PU foam	95075 ± 257	180229 ± 830	-	1.90 ± 0.01	-
	Sample rings[a]	-	-	-	1.82 ± 0.08	1.62 ± 0.06
P12.1	PU foam/boulder[b]	88959 ± 326	-	-	-	-
P13	PU foam	4162 ± 72	6429 ± 2	6272 ± 1	1.54 ± 0.03	1.51 ± 0.03
	Sample rings[a]	-	-	-	1.39 ± 0.09	1.35 ± 0.09

[a] Mean values of multiple (BD17-P11: 8, BD17-P12: 6, BD17-P13: 3) measurements using 100 cm³ soil sample rings.

[b] Volume of a boulder (6116 ± 63 cm³) placed into the respective pits subtracted from PU foam-derived volume.

Table 4. Imaging scenarios, photogrammetry-derived volumes (V_{SfM}), excavation weights (field state; $m_{e,f}$) and field bulk densities ($\rho_{B,f}$) of the standard pits BD17-P01, -P06, -P11, -P12 and -P13.

ID	Elevation (m a.s.l.)[a]	Workflow	Camera	Lighting Pre-dug	Lighting Pit	V_{SfM} (cm³)[b]	Dif. (%)[c]	$m_{e,f}$ (g)[d]	$\rho_{B,f}$ (g cm⁻³)	Difference (g cm⁻³)[c]	(%)[c]
P01	86	Perf.	DSLM	Sunny/ cloudy	Sunny/ cloudy	7633 ± 70	-0.7	16282 ± 2	2.13 ± 0.02	+0.01	+0.7
		Perf.	Smartphone			7698 ± 124	+0.2		2.11 ± 0.03	-0.00	-0.1
		Freew.	DSLM			7672 ± 203	-0.1		2.12 ± 0.06	+0.00	+0.1
		Freew.	Smartphone			7012 ± 281	-8.7		2.32 ± 0.09	+0.20	+9.6
P06	84	Perf.	DSLM	Sunny/ cloudy	Sunny/ cloudy	8572 ± 70	+1.5	17872 ± 2	2.08 ± 0.02	-0.03	-1.5
		Perf.	Smartphone			8576 ± 124	+1.6		2.08 ± 0.03	-0.03	-1.6
		Freew.	DSLM			8048 ± 203	-4.7		2.22 ± 0.06	+0.10	+4.9
		Freew.	Smartphone			7995 ± 281	-5.3		2.24 ± 0.08	+0.12	+5.6
P11m	86	Perf.	DSLM	Cloudy/ sunny	Sunny	108871 ± 70	+9.0	233489 ± 830	2.14 ± 0.01	-0.19	-8.2
		Perf.	Smartphone			110955 ± 124	+11.1		2.10 ± 0.01	-0.23	-10.0
		Freew.	DSLM			108434 ± 203	+8.5		2.15 ± 0.01	-0.18	-7.9
		Freew.	Smartphone			108077 ± 281	+8.2		2.16 ± 0.01	-0.18	-7.6
P11a		Perf.	DSLM		Fully shaded	110386 ± 70	+10.5		2.12 ± 0.01	-0.22	-9.5
		Perf.	Smartphone			111064 ± 124	+11.2		2.10 ± 0.01	-0.23	-10.0
		Freew.	DSLM			113650 ± 203	+13.8		2.05 ± 0.01	-0.28	-12.1
		Freew.	Smartphone			112265 ± 281	+12.4		2.08 ± 0.01	-0.26	-11.0
P12m	89	Perf.	DSLM	Fully shaded	Sunny	92844 ± 70	-2.3	180229 ± 830	1.94 ± 0.01	+0.05	+2.4
		Perf.	Smartphone			91095 ± 124	-4.2		1.98 ± 0.01	+0.08	+4.4
		Freew.	DSLM			91149 ± 203	-4.1		1.98 ± 0.01	+0.08	+4.3
		Freew.	Smartphone			90660 ± 281	-4.6		1.99 ± 0.01	+0.09	+4.9
P12a		Perf.	DSLM		Partly shaded	94376 ± 70	-0.7		1.91 ± 0.01	+0.01	+0.7
		Perf.	Smartphone			91732 ± 124	-3.5		1.96 ± 0.01	+0.07	+3.6
		Freew.	DSLM			91104 ± 203	-4.2		1.98 ± 0.01	+0.08	+4.4
		Freew.	Smartphone			93877 ± 281	-1.3		1.92 ± 0.01	+0.02	+1.3
P13	94	Perf.	DSLM	Sunny/ cloudy	Sunny/ cloudy	4481 ± 70	+7.7	6429 ± 2	1.43 ± 0.02	-0.11	-7.1
		Perf.	Smartphone			4452 ± 124	+7.0		1.44 ± 0.04	-0.10	-6.5
		Freew.	DSLM			4340 ± 203	+4.3		1.48 ± 0.07	-0.06	-4.1
		Freew.	Smartphone			4135 ± 281	-0.6		1.55 ± 0.11	+0.01	+0.6

[a] All samples taken within a radius of ~50 m (50.9972°N, 6.4345°E).

[b] Uncertainties are 1σ as obtained from the tests performed on the artificial pit (see Table 2).

[c] Difference between modelled volumes/densities and reference values (see Table 3).

 [d] Errors based on balance accuracy. The accuracy of the hand balance used here to lift the excavated material of BD17-P11 and -P12 and the tarp was determined to be about ±260 g by comparing test measurements with those obtained from an ordinary balance (d = 1 g) in the laboratories of the University of Cologne. The latter balance was further used to determine the mass of the excavations of BD17-P01, -P06 and –P13.

Table 5. Imaging scenarios and SfM-MVS photogrammetry-derived volumes of the modified pits BD17-P11.1, -P12.1 (V_{SfM}) and the resulting boulder volumes ($V_{b,SfM}$).

ID	Workflow	Camera	Lighting Pre-dug	Lighting Pit	V_{SfM} (cm^3)[a]			Dif. (%)[b,c]	$V_{b,SfM}$ (cm^3)[d]			Dif. (%)
P11.1m	Perf.	DSLM	Cloudy/ sunny	Sunny	104736	±	70	+11.7	4135	±	99	-32.4
		Smartphone			n.d.[e]			n.d.[e]	n.d.[e]			n.d.[e]
	Freew.	DSLM			101217	±	203	+7.9	7217	±	287	+18.0
		Smartphone			n.d.[e]			n.d.[e]	n.d.[e]			n.d.[e]
P11.1a	Perf.	DSLM		Fully shaded	104059	±	70	+11.0	6326	±	99	+3.4
		Smartphone			104835	±	124	+11.8	6229	±	175	+1.8
	Freew.	DSLM			108269	±	203	+15.4	5381	±	287	-12.0
		Smartphone			106934	±	281	+14.0	5331	±	397	-12.8
P12.1m	Perf.	DSLM	Fully shaded	Sunny	85774	±	70	-8.5	7071	±	99	+15.6
		Smartphone			84698	±	124	-9.7	6397	±	175	+4.6
	Freew.	DSLM			89958	±	203	-4.1	1191	±	287	-80.5
		Smartphone			85150	±	281	-9.2	5510	±	397	-9.9
P12.1a	Perf.	DSLM		Partly shaded	86860	±	70	-7.4	7517	±	99	+22.9
		Smartphone			85566	±	124	-8.8	6166	±	175	+0.8
	Freew.	DSLM			87093	±	203	-7.1	4011	±	287	-34.4
		Smartphone			84191	±	281	-10.2	9686	±	397	+58.4

[a] **Uncertainties are 1σ as obtained from the tests performed on the artificial pit (see Table 2).**

[b] **Difference between modelled volumes/densities and reference values (see Table 3).**

925   [c] **Reference volume calculated by subtracting the reference value for $V_{b,ref}$ (6116 ± 63 cm^3) from the PU foam/polystyrene casts-derived reference volumes V_{PU}.**

[d] **Derived by subtracting the volumes of the standard pits from the corresponding modified pits.**

[e] **Not determined.**

930

935

940

945

Table 6. Field-state bulk density ($\rho_{B,f}$) consistency and precision control for AT17/18 samples.

Sample ID	Exposition	Location (°)		Elevation (m a.s.l)[a]	z (cm)[b]	$m_{e,f}$ (g)[c]	V_{SfM} (cm^3)[d]	$\rho_{B,f}$ (g cm^{-3})
AT17-001	Ridgetop	-30.4613	-71.6522	338	0 - 22	11150 ± 71	8559 ± 70	1.30 ± 0.01
					22 - 28	3400 ± 71	2238 ± 70	1.52 ± 0.06
					0 - 28	14550 ± 100	10748 ± 70	1.35 ± 0.01
AT17-028	Ridgetop	-30.4660	-71.6487	387	0 - 5	10950 ± 71	8562 ± 70	1.28 ± 0.01
					5 - 12	13850 ± 71	7130 ± 70	2.06 ± 0.02
					0 - 12	24800 ± 100	16237 ± 70	1.53 ± 0.01
AT17-029	North	-30.4658	-71.6499	367	0 - 8	8650 ± 71	6940 ± 70	1.25 ± 0.02
					8 - 13	3400 ± 71	2236 ± 70	1.52 ± 0.06
					0 - 13	12050 ± 100	8895 ± 70	1.35 ± 0.02
AT17-032TS[e]	North	-30.4643	-71.6502	324	0 - 5	3400 ± 71	2028 ± 70	1.68 ± 0.07
AT17-032[e]					0 - 10	4650 ± 71	2812 ± 70	1.65 ± 0.05
AT18-102(1)[e]	Ridgetop	-30.3922	-71.6474	428	0 - 28	60400 ± 122	32876 ± 70	1.84 ± 0.01
AT18-102(2)[e]					0 - 3	2150 ± 71	2356 ± 70	0.91 ± 0.04

[a] **DTM-derived.**

[b] **Depth below the surface as measured in the field.**

[c] **Field-state excavation mass measured using a KERN 50K50 hand balance with d = 50 g. The errors shown here include the uncertainty for the mass of the excavated material and that of the tarp.**

[d] **SfM-MVS photogrammetry-based volumes. 1σ uncertainties derived from the testing phase (see Table 2; performance workflow).**

[e] **Measurements from two pits that were dug directly next to each other (~1 m).**

Table 7. Average values derived for the soil depth (z) and photogrammetry-based field-state bulk density ($\rho_{B,f}$) determination of the AT17/18 sampling sites.

Catchment	Exposition	n	z (cm)[a]	$m_{e,f}$ (g)[b]	V_{SfM} (cm^3)[b]	$\rho_{B,f}$ (g cm^{-3})[b]
C1	North	10	8 ± 4	8640 ± 3993	6046 ± 3051	1.49 ± 0.17
	South	9	19 ± 7	17261 ± 12765	13971 ± 11163	1.31 ± 0.18
C2	North	12	20 ± 7	21845 ± 7094	13354 ± 4112	1.63 ± 0.14
	South	10	23 ± 5	35280 ± 9152	24209 ± 6799	1.47 ± 0.12
C5	North	11	12 ± 5	13491 ± 7234	9055 ± 4848	1.47 ± 0.19
	South	10	16 ± 9	16986 ± 9138	12093 ± 6607	1.43 ± 0.17
Ridgetops (c. divides)		8	11 ± 8	15567 ± 9093	10170 ± 5288	1.49 ± 0.29

[a] **Depth below the surface as measured in the field.**

[b] **Uncertainties reported for the excavated mass (field state; $m_{e,f}$) and the SfM-MVS photogrammetry-based excavation volume (V_{SfM}) denote 1σ of the mean value without considering individual measurement errors.**

Table B1. Time required to derive watertight models of the soil pits for both workflows and all cameras applied.

Sites	Camera	Workflow	Mean processing duration	
			Total (min)	Manual[a] (min)
D01-D16	DSLM	Performance	28	16
		Freeware	27	8
D17-D26	Smartphone	Performance	25	14
		Freeware	30	8
P01-P13	DSLM	Performance	53	26
		Freeware	85	17
	Smartphone	Performance	68	32
		Freeware	84	17
AT17/18[b]	DSLM[c]	Performance	57	31

[a] **Includes the semi-automated referencing via placing markers in Agisoft Metashape.**

[b] **Computing performed on a consumer-grade computer (years 2019/2020).**

970 [c] **Two different camera models used (both with 16 MP resolution).**

Table B2. Comparison of field-state ($\rho_{B,f}$) and dry bulk densities ($\rho_{B,d}$) for the different workflows and cameras tested.

ID	Workflow	Camera	$m_{e,f}$ (g)[a]		$m_{e,d}$ (g)[b]		$\rho_{B,f}$ (g cm^{-3})[c]			$\rho_{B,d}$ (g cm^{-3})[c]		
P01	Performance	DSLM	16282	± 2	15686	± 2	2.13	±	0.02	2.06	±	0.02
		Smartphone					2.11	±	0.03	2.04	±	0.03
	Freeware	DSLM					2.12	±	0.06	2.04	±	0.05
		Smartphone					2.32	±	0.09	2.24	±	0.09
P06	Performance	DSLM	17872	± 2	17585	± 1	2.08	±	0.02	2.05	±	0.02
		Smartphone					2.08	±	0.03	2.05	±	0.03
	Freeware	DSLM					2.22	±	0.06	2.19	±	0.06
		Smartphone					2.24	±	0.08	2.20	±	0.08
P13	Performance	DSLM	6429	± 1	6272	± 1	1.43	±	0.02	1.40	±	0.02
		Smartphone					1.44	±	0.04	1.41	±	0.04
	Freeware	DSLM					1.48	±	0.07	1.45	±	0.07
		Smartphone					1.55	±	0.11	1.52	±	0.10

[a] **Field-state excavation mass.**

[b] **Oven-dried excavation mass.**

975 [c] **Uncertainties include the 1σ uncertainty in volume as obtained from the tests performed on the artificial pit and the accuracy of the balance used.**

980

Table B3. Samples from sample rings taken at sites BD17-P11, -P12 and –P13.

ID	z (cm)[a]	$m_{e,f}$ (g)[b]	$m_{e,d}$ (g)[c]	$\rho_{B,f}$ (g cm^{-3})[d]	$\rho_{B,d}$ (g cm^{-3})[e]
BD17-P11.S1	8	155.64 ± 0.01	147.78 ± 0.01	1.56 ± 0.01	1.48 ± 0.01
BD17-P11.S2	20	175.66 ± 0.01	168.39 ± 0.01	1.76 ± 0.01	1.68 ± 0.01
BD17-P11.S3	28	165.25 ± 0.01	158.93 ± 0.01	1.65 ± 0.01	1.59 ± 0.01
BD17-P11.S4	35	171.40 ± 0.01	163.58 ± 0.01	1.71 ± 0.01	1.64 ± 0.01
BD17-P11.S5	4	173.31 ± 0.01	146.49 ± 0.01	1.73 ± 0.01	1.46 ± 0.01
BD17-P11.S6	17	188.13 ± 0.01	161.69 ± 0.01	1.88 ± 0.01	1.62 ± 0.01
BD17-P11.S7	28	183.92 ± 0.01	175.72 ± 0.01	1.84 ± 0.01	1.76 ± 0.01
BD17-P11.S8	33	163.55 ± 0.01	157.88 ± 0.01	1.64 ± 0.01	1.58 ± 0.01
BD17-P12.S1	6	166.98 ± 0.01	151.58 ± 0.01	1.67 ± 0.01	1.52 ± 0.01
BD17-P12.S2	23	186.00 ± 0.01	166.05 ± 0.01	1.86 ± 0.01	1.66 ± 0.01
BD17-P12.S3	38	178.12 ± 0.01	155.52 ± 0.01	1.78 ± 0.01	1.56 ± 0.01
BD17-P12.S4	7	187.44 ± 0.01	166.93 ± 0.01	1.87 ± 0.01	1.67 ± 0.01
BD17-P12.S5	20	186.47 ± 0.01	164.41 ± 0.01	1.86 ± 0.01	1.64 ± 0.01
BD17-P12.S6	35	188.31 ± 0.01	166.54 ± 0.01	1.88 ± 0.01	1.67 ± 0.01
BD17-P13.S1	-[f]	143.40 ± 0.01	136.1 ± 0.01	1.43 ± 0.01	1.36 ± 0.01
BD17-P13.S2	-[f]	126.55 ± 0.01	119.99 ± 0.01	1.27 ± 0.01	1.20 ± 0.01
BD17-P13.S3	-[f]	147.93 ± 0.01	141.96 ± 0.01	1.48 ± 0.01	1.42 ± 0.01

[a] **Depth below the surface.**

[b] **Field-state excavation mass.**

[c] **Oven-dried excavation mass.**

[d] **Field-state bulk density.**

[e] **Dry bulk density.**

[f] **Samples taken a few centimetres above, to the right and to the left of the cavity.**